

Evidence for plunging river plume deposits in the Pahrump Hills member of the Murray formation, Gale crater, Mars

KATHRYN M. STACK* , JOHN P. GROTZINGER†, MICHAEL P. LAMB†, SANJEEV GUPTA‡, DAVID M. RUBIN§, LINDA C. KAH¶ , LAUREN A. EDGAR** , DEIRDRA M. FEY†† , JOEL A. HUROWITZ‡‡, MARIE MCBRIDE§§, FRANCES RIVERA-HERNÁNDEZ¶¶ , DAWN Y. SUMNER***, JASON K. VAN BEEK††, REBECCA M. E. WILLIAMS††† and ROBIN AILEEN YINGST†††

*Jet Propulsion Laboratory, California Institute of Technology, 4800 Oak Grove Drive, Pasadena, CA 91109, USA (E-mail: kathryn.m.stack@jpl.nasa.gov)

†California Institute of Technology, 1200 East California Boulevard, Pasadena, CA 91125, USA

‡Imperial College London, Kensington, London SW7 2AZ, UK

§University of California Santa Cruz, 1156 High Street, Santa Cruz, CA 95064, USA

¶University of Tennessee, 1621 Cumberland Avenue, Knoxville, TN 37996, USA

**USGS Astrogeology Science Center, 2255 N. Gemini Drive, Flagstaff, AZ 86001, USA

††Malin Space Science Systems, 5880 Pacific Center Boulevard, San Diego, CA 92121, USA

‡‡Stony Brook University, 100 Nicolls Road, Stony Brook, NY 11794, USA

§§Purdue University, 550 Stadium Mall Drive, West Lafayette, IN 47907, USA

¶¶Dartmouth College, 6105 Fairchild Hall, Hanover, NH 03755, USA

***UC Davis, 1 Shields Avenue, Davis, CA 95616, USA

†††Planetary Science Institute, 1700 E. Lowell, Suite 106, Tucson, AZ 85719, USA

Associate Editor – Nicholas Tosca

ABSTRACT

Recent robotic missions to Mars have offered new insights into the extent, diversity and habitability of the Martian sedimentary rock record. Since the *Curiosity* rover landed in Gale crater in August 2012, the Mars Science Laboratory Science Team has explored the origins and habitability of ancient fluvial, deltaic, lacustrine and aeolian deposits preserved within the crater. This study describes the sedimentology of a *ca* 13 m thick succession named the Pahrump Hills member of the Murray formation, the first thick fine-grained deposit discovered *in situ* on Mars. This work evaluates the depositional processes responsible for its formation and reconstructs its palaeoenvironmental setting. The Pahrump Hills succession can be subdivided into four distinct sedimentary facies: (i) thinly laminated mudstone; (ii) low-angle cross-stratified mudstone; (iii) cross-stratified sandstone; and (iv) thickly laminated mudstone–sandstone. The very fine grain size of the mudstone facies and abundant millimetre-scale and sub-millimetre-scale laminations exhibiting quasi-uniform thickness throughout the Pahrump Hills succession are most consistent with lacustrine deposition. Low-angle geometric discordances in the mudstone facies are interpreted as ‘scour and drape’ structures and suggest the action of currents, such as those associated with hyperpycnal river-generated plumes plunging into a lake. Observation of an overall upward coarsening in grain size and thickening of laminae throughout the Pahrump Hills succession is consistent with deposition from basinward progradation of a fluvial-deltaic system derived from the northern crater rim into the Gale crater lake. Palaeohydraulic modelling constrains the salinity of the ancient lake in Gale crater: assuming river sediment concentrations typical of floods on Earth, plunging river plumes and sedimentary

structures like those observed at Pahrump Hills would have required lake densities near freshwater to form. The depositional model for the Pahrump Hills member presented here implies the presence of an ancient sustained, habitable freshwater lake in Gale crater for at least $ca\ 10^3$ to 10^7 Earth years.

Keywords *Curiosity* rover, Gale crater, lacustrine, Mars, Mars Science Laboratory, sedimentology, stratigraphy.

INTRODUCTION

Ancient lake deposits are among the most attractive astrobiology targets for *in situ* rover and lander missions to Mars. Environments containing long-lived surface water could have once hosted life and may be conducive for the concentration and preservation of organic matter (Farmer & DesMarais, 1999; Summons *et al.*, 2011; Hays *et al.*, 2017). Observations from ground-based and orbital missions to Mars demonstrate the presence of a widespread sedimentary rock record exposed on the Martian surface (Sharp, 1973; Malin & Edgett, 2000; Grotzinger & Milliken, 2012; Stack, 2015; Rogers *et al.*, 2018), including evidence that water may have persisted on the Martian surface for geologically significant timescales. The presence of ancient deltas (Fassett & Head, 2005; Lewis & Aharonson, 2006; Ehlmann *et al.*, 2008; Di Achille & Hynek, 2010; Ansan *et al.*, 2011; Schon *et al.*, 2012; Rice *et al.*, 2013; DiBiase *et al.*, 2013; Morgan *et al.*, 2018; Goudge *et al.*, 2018), sublacustrine fans (Dromart *et al.*, 2007; Metz *et al.*, 2009), putative shorelines (Parker *et al.*, 1989; Parker *et al.*, 1993; Clifford & Parker, 2001; Peron *et al.*, 2007) and hundreds of candidate crater lake basins (Goldspiel & Squyres, 1991; Cabrol & Grin, 1999, 2001; Fassett & Head, 2008; Warner *et al.*, 2010; Goudge *et al.*, 2012) observed in orbital datasets help to support this interpretation. However, clear evidence for *in situ* lacustrine deposits requires ground-based surface observations.

A subset of possible Martian crater lake basins has been interpreted to contain ancient lacustrine deposits exposed at the surface (Cabrol & Grin, 1999; Malin & Edgett, 2000; Fassett & Head, 2008; Goudge *et al.*, 2012), although only at two sites have such deposits been investigated *in situ* by rover missions. An ejecta block near Santa Maria crater in Meridiani Planum studied by the *Opportunity* rover team was interpreted as possibly lacustrine in origin, although its lack of context made it difficult to

eliminate alternative aeolian depositional hypotheses (Edgar *et al.*, 2014). The Mars Science Laboratory (MSL) Science Team has explored several lacustrine deposits in Gale crater with the *Curiosity* rover. At Yellowknife Bay, a lacustrine origin was favoured for the 1.5 m thick interval of clay-bearing mudstones of the Sheepbed member (Grotzinger *et al.*, 2014). Lacustrine deposits have also been interpreted in the Murray formation, the stratigraphically oldest rocks exposed in the eroded foothills of Aeolis Mons (informally Mount Sharp), the 5 km high central mound within Gale crater (Grotzinger *et al.*, 2015; Fedo *et al.*, 2017, 2018; Rivéra-Hernandez *et al.*, 2018).

The MSL Science Team carried out a detailed examination of the Murray formation at an outcrop named Pahrump Hills (see Appendix S1), a $ca\ 13$ m thick section whose strata have been informally designated as the Pahrump Hills member (Grotzinger *et al.*, 2015). Since the Pahrump Hills member represents the first and oldest continuous exposure of the Murray formation encountered by the rover, the Science Team devoted a six and a half month long campaign to this location with the intention of compiling a reference section for the basal Murray formation. The Science Team used the rover's integrated payload to obtain a dense record of sedimentary structures and textures, together with compositional measurements. This study builds on earlier work by Grotzinger *et al.* (2015), and uses the characterization of grain size, sedimentary structures and stratal geometries to reconstruct sedimentary processes and palaeoenvironments of the lower Murray formation depositional system preserved at Pahrump Hills. This analysis and complementary palaeohydraulic modelling are used to provide stronger constraints on the lacustrine depositional model for the Murray formation exposed at Pahrump Hills than the initial analysis of Grotzinger *et al.* (2015), with new implications for the salinity, longevity and habitability of the ancient Gale crater lake.

GEOLOGICAL SETTING

Gale crater (centred at 5.37°S, 137.81°E), selected as the field site for the *Curiosity* rover (Grotzinger *et al.*, 2012; Golombek *et al.*, 2012), is a *ca* 154 km diameter crater located on Mars' crustal dichotomy boundary (Fig. 1A), a global topographic distinction that separates the ancient, heavily cratered southern highlands from the smooth northern plains of Mars. Gale crater is one of a class of crater basins on Mars that contain thick sedimentary sequences in central mounds (Malin & Edgett, 2000; Grotzinger & Milliken, 2012; Bennett & Bell, 2016; Day *et al.*, 2016). The formation of Gale crater is dated to *ca* 3.6 to 3.8 Ga (Thomson *et al.*, 2011; Le Deit *et al.*, 2013), occurring near the transition between the Late Noachian and Early Hesperian periods. Deposition of crater-filling materials within Gale has been estimated to have begun shortly after the crater's formation, continuing through the Hesperian epoch (Thomson *et al.*, 2011; Le Deit *et al.*, 2013; Grant *et al.*, 2014; Palucis *et al.*, 2014) and possibly into the early Amazonian (Palucis *et al.*, 2014), with deposition interrupted by at least several major periods of erosion resulting in recognizable unconformities within the rock record at Gale crater (Malin & Edgett, 2000; Rossi *et al.*, 2008; Anderson & Bell, 2010; Milliken *et al.*, 2010; Thomson *et al.*, 2011; Le Deit *et al.*, 2013; Fraeman *et al.*, 2016; Kite *et al.*, 2016; Watkins *et al.*, 2016; Banham *et al.*, 2018). Aeolian erosion of crater-filling deposits and spatially isolated but active aeolian sedimentation have continued to the present-day (Day & Kocurek, 2016; Ewing *et al.*, 2017; Bridges & Ehlmann, 2017).

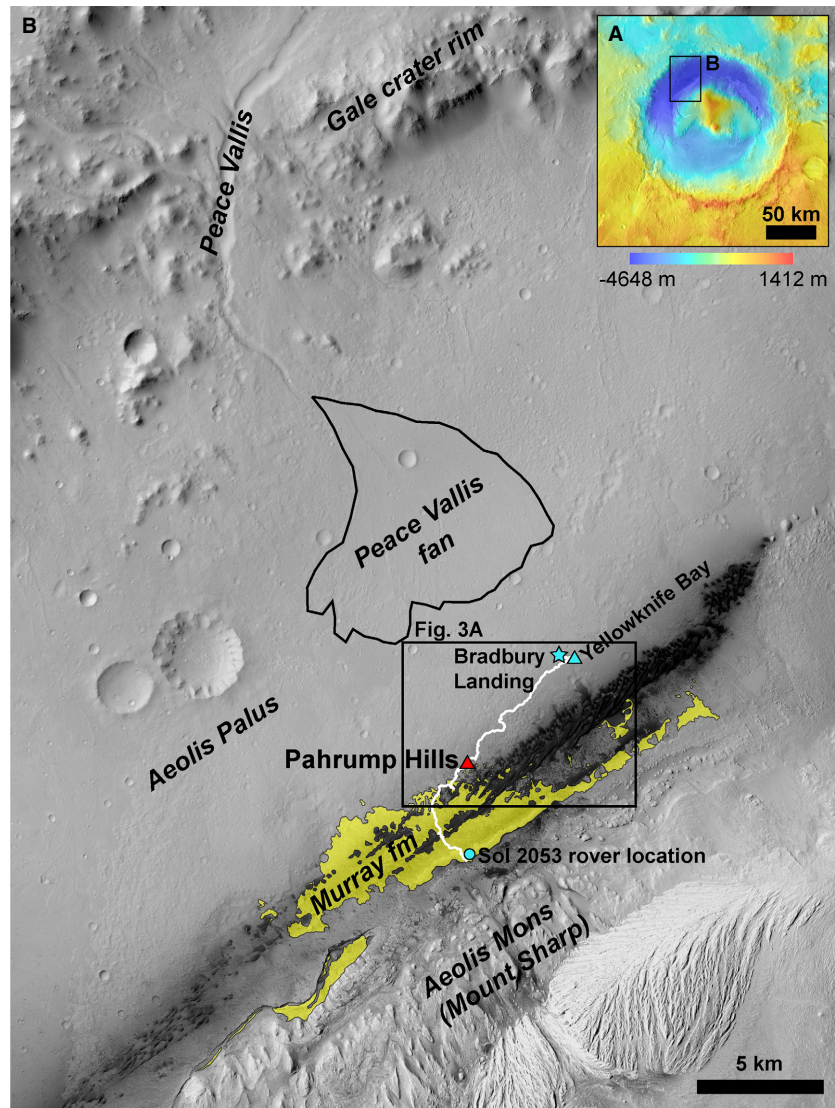
Gale crater contains within it a nearly 5 km high mound of layered strata, Aeolis Mons (Fig. 1A), the stratigraphy of which is interpreted to preserve a record of the evolution of ancient sedimentary processes and environmental changes with implications for the habitability of early Mars (Anderson & Bell, 2010; Milliken *et al.*, 2010; Thomson *et al.*, 2011; Fraeman *et al.*, 2012; Le Deit *et al.*, 2013; Grotzinger *et al.*, 2014). Earlier orbiter data-based interpretations of the Gale rock record included deposition by volcanic (Scott *et al.*, 1978; Scott & Chapman, 1995; Greeley & Guest, 1987; Malin & Edgett, 2000; Bridges *et al.*, 2010; Thomson *et al.*, 2008), aeolian (Anderson & Bell, 2010; Kite *et al.*, 2013; Milliken *et al.*, 2014; Kite *et al.*, 2016), fluvial (Anderson & Bell, 2010) and lacustrine (Cabrol *et al.*, 1999;

Malin & Edgett, 2000) processes, as well as deposition from springs (Rossi *et al.*, 2008; Andrews-Hanna *et al.*, 2012). Ground-based observations acquired by *Curiosity* during the first five years of its mission confirm that deposition of strata exposed on the floor of Gale crater and in the foothills of Aeolis Mons was dominated by sedimentary processes in fluvial, deltaic, lacustrine and aeolian depositional environments (Williams *et al.*, 2013; Vasavada *et al.*, 2014; Grotzinger *et al.*, 2014, 2015; Stack *et al.*, 2016; Rice *et al.*, 2017; Edgar *et al.*, 2017; Banham *et al.*, 2018). Volcanic, spring or surface hydrothermal deposits have not been discovered to date.

Aeolis Palus, the plains that make up the present-day floor of Gale crater, is composed primarily of fluvial and fluvio-deltaic sandstones and conglomerates which have been designated informally as the Bradbury group (Williams *et al.*, 2013; Vasavada *et al.*, 2014; Grotzinger *et al.*, 2015; Stack *et al.*, 2016; Rice *et al.*, 2017; Figs 1B and 2). The occurrence of systematic facies variations, along with the discovery of southward-prograding clinoform deposits over an elevation range of *ca* 80 m led Grotzinger *et al.* (2015) to interpret the Bradbury group as a network of braided rivers flowing south from Gale crater's northern rim. This sediment routing system was capable of transporting cobbles up to *ca* 10 cm in diameter (Williams *et al.*, 2013; Grotzinger *et al.*, 2015; Szabó *et al.*, 2015; Mangold *et al.*, 2016) in water depths estimated to be between 0.03 m and 0.9 m based on the grain-size distribution of conglomerate clasts (Williams *et al.*, 2013). These rivers were interpreted by Grotzinger *et al.* (2015) to have fed a series of metre to decametre-scale stacked delta mouth bars composed of dipping clinoforms that prograded towards the south. A natural prediction of this depositional model was that *Curiosity* should encounter distal basinal lacustrine facies, the lateral facies equivalents of these proximal fluvio-deltaic deposits, as it continued to traverse basinward to the south (Grotzinger *et al.*, 2015).

Aeolis Palus is bounded to the south by a distinct topographic break in slope *ca* 10 m high. The Murray formation, the basal exposed unit within the stratigraphic succession of Aeolis Mons, is exposed south of this topographic break and is mappable in orbiter-derived visible images for *ca* 30 km along the base of Aeolis Mons (Figs 1B and 3A). The Murray formation

Fig. 1. (A) Gale crater viewed in a Mars Odyssey Thermal Emission Imaging Systems (THEMIS) daytime infrared basemap draped with topography from the Mars Global Surveyor Mars Orbiter Laser Altimeter (MOLA) topography. (B) *Curiosity's* field site in Gale crater. The white line marks the rover's traverse from Bradbury Landing to the Sol 2053 position. The extent of the Murray formation recognized in orbital images (shown in yellow) was mapped on a Context Camera (CTX) basemap at a scale of 1 : 15 k.



is distinguished in visible orbital images by its bright to intermediate tone, massive to subtly layered appearance, the presence of metre-scale polygonal fractures throughout, and its relative inability to retain craters compared to surrounding units (Malin and Edgett, 2000; Malin & Edgett, 2000; Anderson & Bell, 2010; Milliken *et al.*, 2010; Thomson *et al.*, 2011; Grotzinger *et al.*, 2015; Fraeman *et al.*, 2016). Analysis of orbiter-derived visible to near-infrared spectroscopic data indicates the presence of hematite, hydrated silica, phyllosilicates and sulphates throughout the Murray formation (Milliken *et al.*, 2010; Fraeman *et al.*, 2016).

Pahrump Hills is a *ca* 225 m long outcrop located along the boundary between Aeolis Palus and the northern contact of the Murray formation, at the southern end of Amargosa

valley (Fig. 3). The Pahrump Hills member exposed here represents the northernmost, lowest elevation, and likely stratigraphically oldest exposure of the Murray formation encountered by the rover (Figs 1B and 3A). As viewed in images from the High Resolution Imaging Science Experiment (HiRISE) onboard the Mars Reconnaissance Orbiter, Pahrump Hills strata are partially isolated from the main exposure of the Murray formation by strata interpreted to be overlying Stimson formation (Calef *et al.*, 2013; Grotzinger *et al.*, 2015; Watkins *et al.*, 2016; Stack *et al.*, 2017; Kronyak *et al.*, 2017; Banham *et al.*, 2018), a younger aeolian sandstone unit interpreted to unconformably overlie the Murray formation (Watkins *et al.*, 2016; Banham *et al.*, 2018; Figs 2 and 3B).

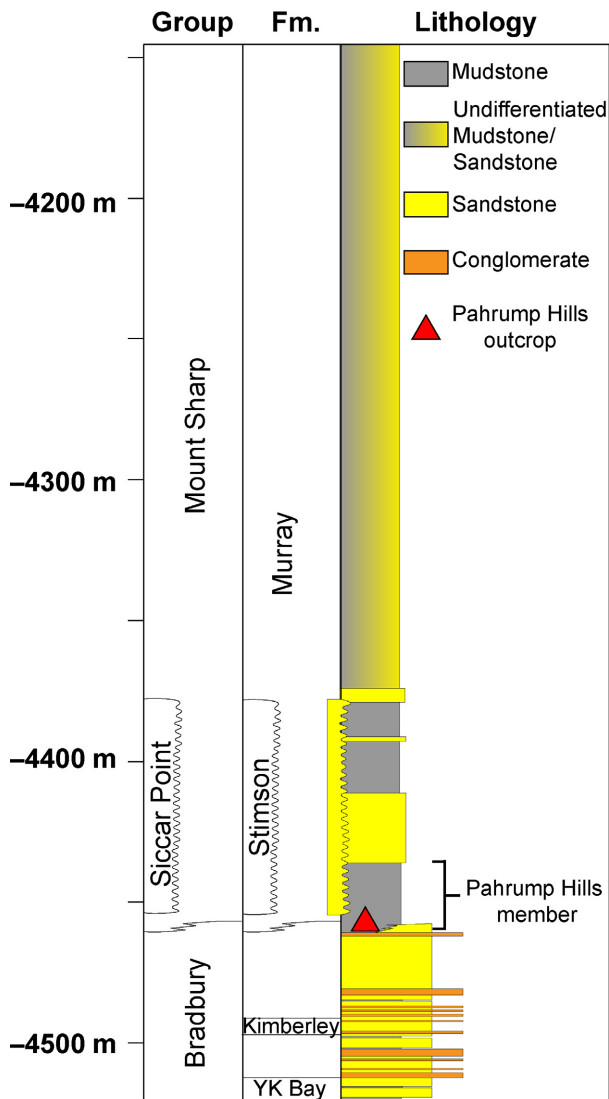


Fig. 2. Schematic stratigraphic column of the sequence of rocks explored by the *Curiosity* rover team in Gale crater [after Grotzinger *et al.* (2015) and Fedo *et al.* (2017)].

DATA AND METHODS

The Pahrump Hills campaign

The MSL Science Team devoted six and a half months (Sols 753 to 923, where ‘Sol’ denotes the designated Martian day of the MSL mission) to a detailed investigation of the Pahrump Hills outcrop with the aim of characterizing a reference section for the basal Murray formation. The first drill sample of the Murray formation (Confidence Hills) was acquired on Sol 759 shortly after arriving at the base of Pahrump Hills (Fig. 3C and D). Drilling was followed by

reconnaissance characterization of the Pahrump Hills outcrop (Sols 780 to 794, Loop 1) during which the rover was commanded to make observations using only its remote sensing instruments [Mast Camera (Mastcam), Chemistry Camera (ChemCam), Mars Descent Imager (MARDI) and Navigation cameras (Navcam)] at predetermined locations (Fig. 3C). Observations from this reconnaissance traverse were used to select locations for a second traverse of the outcrop (Sols 805 to 862, Loop 2; Fig. 3C and D), during which the team employed the *Curiosity* dust removal tool (DRT) and contact science instruments [Mars Hand Lens Imager (MAHLI) and the Alpha Particle X-ray Spectrometer (APXS)] to acquire fine-scale textural and bulk geochemistry observations. Observations from the first and second loops of the Pahrump Hills ‘walkabout’ were synthesized to inform selection of two additional drill locations, Mojave and Telegraph Peak, on Sols 882 and 908, respectively (Fig. 3C and D). *Curiosity* drove away from the Telegraph Peak drill location on Sol 923 marking the end of the Pahrump Hills campaign.

Instruments and data

Sedimentary facies observed at Pahrump Hills were characterized in this study using images from the *Curiosity* Navcam (Maki *et al.*, 2012), Mastcam (Bell *et al.*, 2017; Malin *et al.*, 2017), ChemCam remote micro-imager (RMI; Maurice *et al.*, 2012; Le Mouélic *et al.*, 2015) and MAHLI (Edgett *et al.*, 2012; Edgett *et al.*, 2015; McBride *et al.*, 2015) cameras. The Navcam, Mastcam and ChemCam instrument suites are located on the *Curiosity* rover Remote Sensing Mast, mounted *ca* 2 m above the surface, and MAHLI is mounted on the rover’s deployable arm. The Navcam stereo mosaics orthorectified to a HiRISE basemap and digital elevation model were used in this study to localize outcrops examined at Pahrump Hills, and to determine the stratigraphic position of outcrops based on absolute differences in elevation. Colour mosaics from the 34 mm (M-34) and 100 mm (M-100) fixed-focal-length Mastcams were used to characterize laminations, sedimentary structures, grain size and the nature of geological contacts. At a 2 m distance, the M-34 and M-100 cameras can achieve resolutions of $440 \mu\text{m pixel}^{-1}$ and *ca* $150 \mu\text{m pixel}^{-1}$ (medium to coarse sand), respectively (Malin *et al.*, 2017). The ChemCam RMI provides focused grey-scale images with a sub-millimetre pixel resolution that can provide

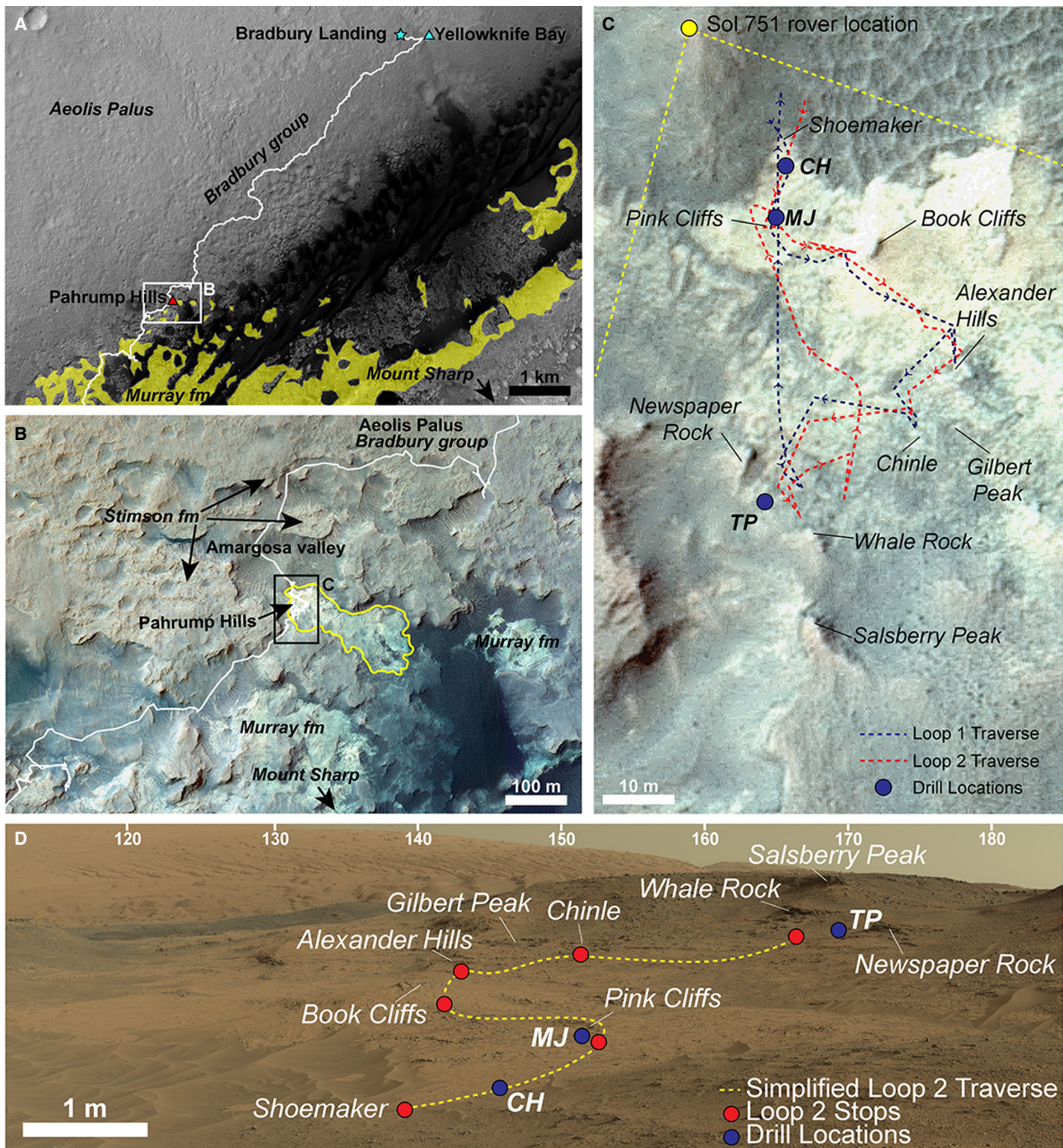


Fig. 3. The location of the Pahrump Hills outcrop. (A) In relation to the *Curiosity* landing site, the rover's traverse through the Bradbury group of Aeolis Palus and the northern extent of the Murray formation (mapped in yellow) shown on a grey-scale High Resolution Imaging Science Experiment (HiRISE) mosaic. (B) Pahrump Hills (outlined in yellow) shown on a colour HiRISE mosaic. Image IDs: ESP_021610_1755 and ESP_033649_1750. White line indicates *Curiosity*'s traverse through the area. (C) The *Curiosity* rover's walkabout strategy at Pahrump Hills annotated with main areas explored by the rover. Yellow dot indicates the rover position when the mosaic in (D) was acquired; dashed yellow lines indicate the ground coverage of the mosaic in (D) in plan view. (D) Main areas explored at Pahrump Hills annotated on a Mastcam M-34 mosaic acquired on Sol 751. Drill location abbreviations: CH, Confidence Hills; MJ, Mojave; TP, Telegraph Peak.

resolution higher than Mastcam, but with a narrower field of view (20 mrad across; 1024×1024 pixels; Maurice *et al.*, 2012; Le Mouélic *et al.*, 2015). This study used ChemCam RMI images of surface targets acquired at distances between 2.1 m and 6.5 m (*ca* 40 to $130 \mu\text{m pixel}^{-1}$, coarse silt to fine sand) from the ChemCam mast unit. Colour images from the MAHLI camera acquired at working distances between 2.6 cm (*ca* $16 \mu\text{m pixel}^{-1}$ resolution) and *ca* 27 cm (*ca* $100 \mu\text{m pixel}^{-1}$ resolution) were used to measure laminae thicknesses, and MAHLI images acquired between 2.6 cm (*ca* $16 \mu\text{m pixel}^{-1}$ resolution, medium silt) and *ca* 9.5 cm (*ca* $40 \mu\text{m pixel}^{-1}$ resolution, coarse silt) working distances were used to characterize grain size, shape and sorting. The Mastcam and MAHLI images employed in this study are non-colour corrected images with a minimal stretch applied to enhance contrast in some cases. The Mastcam images have been perspective or spherically projected.

Lamination thickness and grain-size measurements

The method used in this study to measure lamination thickness is similar to that employed by Hurowitz *et al.* (2017). The thicknesses of individual laminae visible within the MAHLI field of view were measured using the orthogonal distance in pixel units between successive boundaries that define a discernible lamina, then pixel length was converted to a measured distance using the pixel resolution of the corresponding image (Appendix S3, Table S3-1). In this study, only those MAHLI images offering a viewing perspective approximately parallel to bedding were used to minimize the possibility of measuring apparent rather than true lamina thickness, since no correction for lamination dip was applied (Fig. S3-1). It is also unlikely that lamination dip would significantly affect the measured results: even if the laminae dipped 10° , a 2 mm lamina would appear 2.032 mm thick, which is less than 2% error on the measurement. Of the set of MAHLI images used in this study for thickness measurements, only one image location (Telegraph Peak) was also measured by Hurowitz *et al.* (2017). The M-34 images were used previously by Grotzinger *et al.* (2015) to measure lamination thicknesses at Pahrump Hills, but this study uses MAHLI or M-100 (only for the Salsberry Peak location) images

because measured lamination thicknesses are below the pixel resolution of the M-34 camera.

For MAHLI images in which individual grains were resolvable, grain shape, rounding and sorting were classified using the schemes of Blatt *et al.* (1972), Powers (1953) and Harrell (1984), respectively. Grain size was measured via the circular intercept method (Hilliard, 1964) or via grain tracing or diameter measurement when grains were scarce (Appendix S2), and grain size was classified according to the schemes of Wentworth (1922) and Lazar *et al.* (2015). Lazar *et al.* (2015) recommended that very fine-grained rocks composed of at least 50% silt-sized or finer ($<62.5 \mu\text{m}$) grains be referred to generically as 'mudstones'. In this study, as in Grotzinger *et al.* (2015), the term 'mudstone' has been adopted to describe any rock containing 50% or more of its surface area composed of detrital grains unresolvable by the MAHLI camera. Edgett *et al.* (2015) showed that high contrast grains as small as *ca* 30 to $40 \mu\text{m}$ in diameter, *ca* 2 to 3 pixels across in MAHLI images acquired at the smallest working distances, could be resolved in MAHLI images with the appropriate outcrop context. However, the resolvability of grains nearing the pixel resolution limits of the MAHLI camera is highly dependent on surface texture, phase angle, dust or sand cover, the contrast of the individual grains relative to the surrounding rock matrix, and one's confidence in distinguishing clastic grains from secondary diagenetic textures (Yingst *et al.*, 2016).

In this study, grain size assessments were made using MAHLI images taken at working distances between 2.6 cm and 9.5 cm, corresponding to pixel scales between *ca* $16 \mu\text{m}$ and $40 \mu\text{m pixel}^{-1}$. Under ideal lighting, viewing and surface conditions, grains ranging in diameter between $30 \mu\text{m}$ and $80 \mu\text{m}$ (two times pixel scale) should be resolvable in the images used in this study. To account for variability in these conditions, use of the term 'mudstone' in this study implies that the rocks probably are composed predominantly of grains finer than fine sand ($<125 \mu\text{m}$), but quantitative visual assessment of the relative proportion of clay, silt or very fine sand-sized particles within most of the very fine-grained rocks observed at Pahrump Hills is not possible. The ChemCam RMI images were used qualitatively to confirm grain-size observations and measurements made in MAHLI images. An alternative method of determining grain size in the rocks at Pahrump Hills by

Rivéra-Hernández *et al.* (2018) used ChemCam LIBS (Laser Induced Breakdown Spectrometer) data supplemented by MAHLI and ChemCam RMI observations to attempt finer grain-size categorization than that presented here.

SEDIMENTARY FACIES

Facies and subfacies at Pahrump Hills are distinguished on the basis of grain size, sedimentary structures including bedforms, bedding style and thickness, and relative erosional resistance to weathering. Facies are presented in order of increasing grain size. Four distinct sedimentary facies are identified at Pahrump Hills: thinly laminated mudstone, low-angle cross-stratified mudstone, thickly laminated mudstone–sandstone and cross-stratified sandstone (Table 1). Three of these facies were first described by Grotzinger *et al.* (2015) (Table 1): an additional facies, the low-angle cross-stratified mudstone facies, originally included in their thinly laminated mudstone facies is distinguished here. The conglomerate facies observed just prior to *Curiosity's* arrival at Pahrump Hills is not included in this study due to uncertainties in the age and stratigraphic context of the conglomerate relative to the Pahrump Hills member.

Thinly laminated mudstone

The thinly laminated mudstone facies is light grey (for example, Fig. 4A) to reddish-tan (for example, Fig. 4B) in colour on dust-free or brushed surfaces and is uniformly very fine-grained (Fig. 4A to D). Grain size is generally below the resolution of ChemCam RMI images (*ca* 40 to 130 $\mu\text{m pixel}^{-1}$) and the highest resolution Mastcam images (*ca* 150 $\mu\text{m pixel}^{-1}$) examined in this study, although in nearly all of the closest stand-off MAHLI images, clusters of dark pixels typically 2 to 10 pixels across, i.e. coarse silt to fine sand, are discernible (for example, Fig. 4D). Since these dark features, if they are detrital grains, make up less than 50% of the total observable surface area of the rock targets imaged, this facies is most likely to be composed predominantly of silt-sized or finer grains. No obvious grading was observed within this facies in Mastcam, RMI or MAHLI images.

This facies is characterized by the ubiquitous presence of sub-millimetre to millimetre-thick parallel laminations defined by resistant, sometimes knobby and irregularly-shaped ledges

(Fig. 4C). The thinly laminated mudstone facies is divisible into two sub-facies based on laminae continuity, thickness and erosional expression (Fig. 5). The uneven, discontinuously laminated subfacies exhibits laminations of variable thickness that are faintly discernible, but are traceable only over maximum length scales of a few centimetres (Fig. 5A). The rhythmic sub-facies is characterized by laminations exhibiting extremely regular and even thickness that are traceable at least across the field of view of context Mastcam mosaics and often over length scales greater than 1 m (Fig. 5B). Twenty-seven laminae measured within the rhythmic subfacies at the base of Pahrump Hills range in thickness from 0.2 to 0.8 mm, with a mean thickness of 0.5 mm (Shoemaker Pelona target, Figs 6 and S3-1, Table S3-1). Ninety-two laminae measured within the rhythmic subfacies midway through the section range in thickness from 0.4 to 2.2 mm with a mean thickness of 1.4 mm (Telegraph Peak target, Figs 6 and S3-1, Table S3-1).

Sedimentary bedforms and cross-stratification are largely absent from the thinly laminated mudstone facies, with one instance of possible centimetre-scale ripple cross-lamination observed in this facies (Fig. 7). At least two stacked sets of north/north-west dipping foreset laminae were observed at the Book Cliffs area, each approximately 2 cm in height. Foresets appear slightly curved and concave up, indicating asymptotic downlap onto the underlying bounding surfaces. More common in this facies, however, is the occurrence of geometric discordances expressed as the abrupt angular truncation of low-angle inclined subhorizontal laminations (Fig. 8). Lamination dip is difficult to constrain visually, given the general planview exposures of this facies. The observable lateral extent of each truncation surface is limited by the field of view of the Mastcam image (for example, Fig. 8C) or the size of the block in which it was observed (for example, Fig. 8A). The number of laminae truncated by any one surface ranges from about ten to a hundred or more indicating that truncated lamina sets range in thickness from *ca* 1 cm to more than 1 m. Laminae above the truncation surface are always concordant with, and thus drape, the truncation surface.

Low-angle cross-stratified mudstone

The low-angle cross-stratified mudstone facies contains discernible dark grains embedded within a light grey matrix, but these grains make up no

Table 1. Pahrump Hills sedimentary facies.

Grotzinger et al. (2015)	This study	Facies description	Interpretation	Outcrop areas	Relevant target names (Sol #)
Thinly/finely laminated mudstone	Thinly laminated mudstone	Parallel thinly laminated grey to reddish mudstone; consists of rhythmically laminated and uneven, discontinuously laminated subfacies; low-angle geometric discordances observed throughout	Event beds (including scour and drape structures) deposited by plunging plumes in a distal lacustrine setting	Shoemaker Confidence Hills Pink Cliffs Book Cliffs Alexander Hills Telegraph Peak	Pelona; Ricardo (805-806) Maturango (755, 756) – Anaverde (814); Goblin Valley (787, 815) – Calico Mountain (837)
	Low-angle cross-stratified mudstone	Thinly laminated grey mudstone exhibiting variably dipping low-angle cross-stratification	Froude-supercritical bars or bedforms deposited in a sublacustrine channel in a basin margin lacustrine setting	Chinle Gilbert Peak	Goldstone (830-832)
Thickly laminated mudstone–siltstone	Thickly laminated mudstone–sandstone	Thick laminations composed of dark grey sandstone and mudstone	Event beds deposited by plunging plumes in a proximal lacustrine setting	Salsberry Peak Kanosh	– Little Devil; Devil's Punchbowl (942-943)
Cross-laminated sandstone	Cross-stratified sandstone	Dune and ripple cross-stratified sandstone composed of coarse silt to coarse sand-sized white/tan grains within a dark grey, fine-grained matrix	Climbing dune-scale and ripple-scale bedforms deposited in a sublacustrine channel in a proximal basin margin setting	Upper Chinle Whale Rock Newspaper Rock	– Sierra Nevada (854, 860) –
Conglomerate	–	–	–	–	–

more than a few percent of the visible surface area (Fig. 9). Grains range in size from *ca* 40 μm to *ca* 115 μm (silt to very fine sand, Table S2-3), with most grains falling within the coarse silt size range (*ca* 30 to 60 μm , Fig. 9C). Two-hundred and thirty-two individual laminae within this facies range in thickness from *ca* 0.3 to 3.0 mm, with an average thickness of 0.6 mm and a mode of 0.5 mm (Chinle area, Figs 6 and S3-1, Table S3-1). Laminae are traceable up to *ca* 2 m laterally, although most laminations can be traced confidently only over several tens of centimetres due to discontinuity of outcrop exposure.

The low-angle cross-stratified mudstone facies is characterized by inclined laminae exhibiting apparent dips $<10^\circ$ that sometimes show very even, regular thickness (Fig. 10). Laminations form sets ranging from *ca* 5 to 12 cm in

thickness in which laminae downlap onto underlying truncation surfaces that appear to dip $<5^\circ$ (Fig. 11A and B). Apparent dip directions of lamina sets are variable, with dip directions appearing to reverse relative to the immediately underlying set (Fig. 11A and B). Variably dipping laminations sometimes form cross-stratified sets measuring up to *ca* 1.0 to 1.5 m in width and *ca* 20 to 30 cm in height (Fig. 11B and C), suggesting dune-scale three-dimensional bedforms. In one case, laminations form a structure measuring *ca* 10 cm in width with laminations that appear to transition laterally from concave up to concave down (Fig. 11D), providing additional evidence for the presence of three-dimensional bedforms within this facies. Laminae thicknesses remain constant throughout the curvature of the cross-strata.

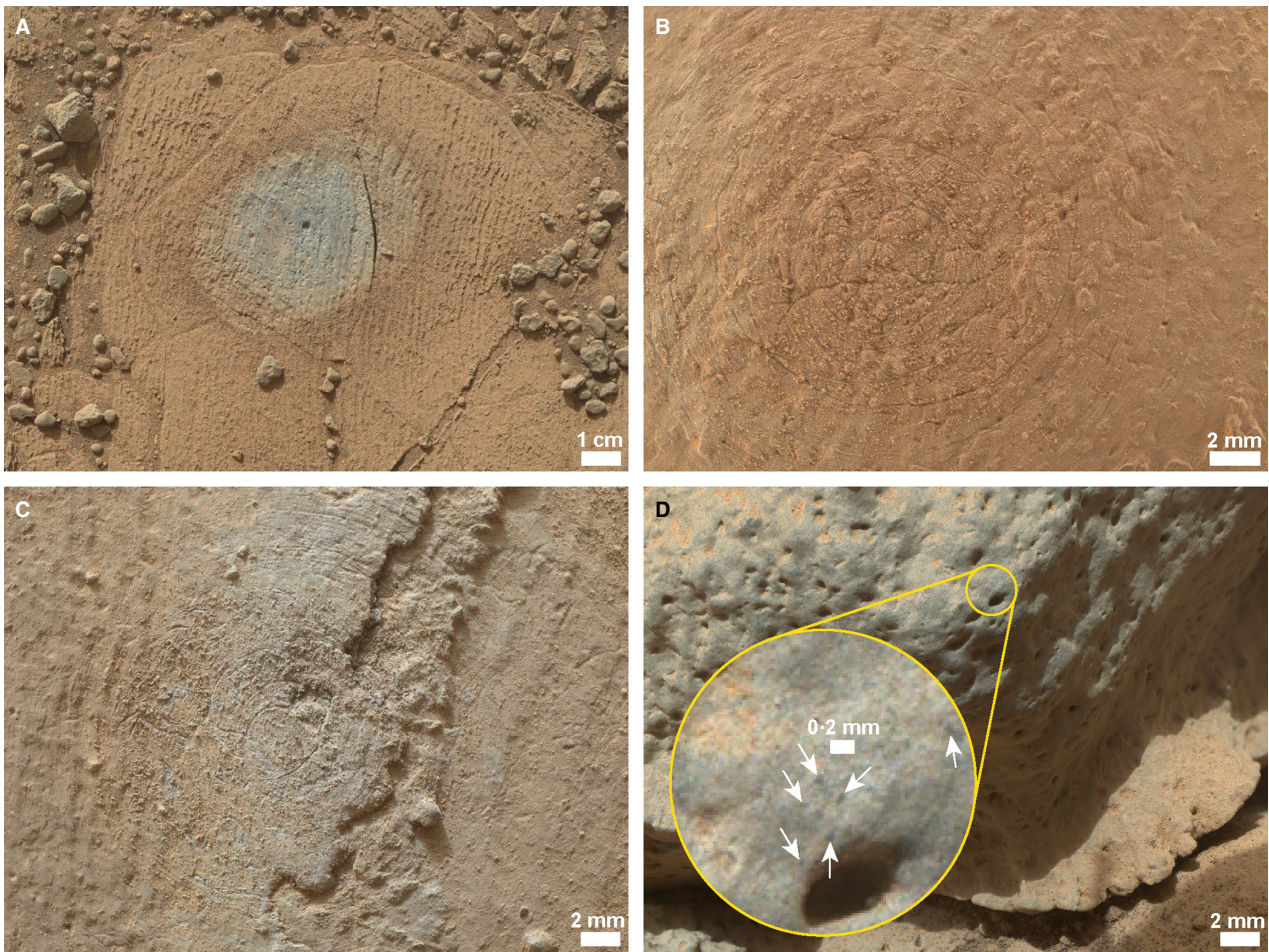


Fig. 4. Mars Hand Lens Imager (MAHLI) images of brushed thinly laminated mudstone facies observed at: (A) Telegraph Peak (MAHLI image 0905MH0001900010302821C00) showing the grey colour of brushed bedrock and the thin laminations, (B) Maturango target at Confidence Hills (MAHLI z-stack 0755MH0001930000204562R00) showing the red colour of brushed bedrock, indentations made by the brush bristles, surface roughness and lack of clearly defined clasts, (C) Ricardo target at Shoemaker (MAHLI z-stack 0806MH0004420000300695R00) showing the grey colour of brushed bedrock, brush indentations and laminations, and unbrushed outcrop observed at (D) Anaverde target at Book Cliffs (MAHLI z-stack 0814MH0001810000301371R00). White arrows point to possible dark silt to very fine sand-sized grains.

Thickly laminated mudstone–sandstone

The thickly laminated mudstone–sandstone facies is dark grey in colour on dust-free surfaces and exhibits specular reflection giving some facets a bright and shiny appearance (Fig. 12B and D). Weathered surfaces exhibit abundant pits filled with reddish-brown dust (Fig. 12C). Most pits are well-rounded and circular or sub-circular in shape, although rare pits appear polygonal and nearly square-shaped (Fig. 12C). Visible *in situ* grains, whose relief is flush with the outcrop surface, are distinguished by well-defined boundaries and a lighter grey colour compared to the dark grey matrix, although they are not observed to be uniformly present throughout the rock

(Fig. 12D). Measurement of 83 grains reveals that the majority are circular, well-sorted and extremely well-rounded, with long axes, taken to represent grain diameter, ranging from 200 μm to 1 mm (fine to coarse sand; Fig. S2-1, Table S2-1). Grains are clast-supported. Individual grains are not resolvable within the dark grey matrix suggesting a grain size of very fine sand or finer.

Planar laminae are most prominently expressed on weathered surfaces and are discernible due to alternations in relative resistance to weathering (Fig. 13). The expression of laminae may be due to changes in the relative proportion of sand-sized or mud-sized grains present within or between laminae, but distinct sand–mud couplets

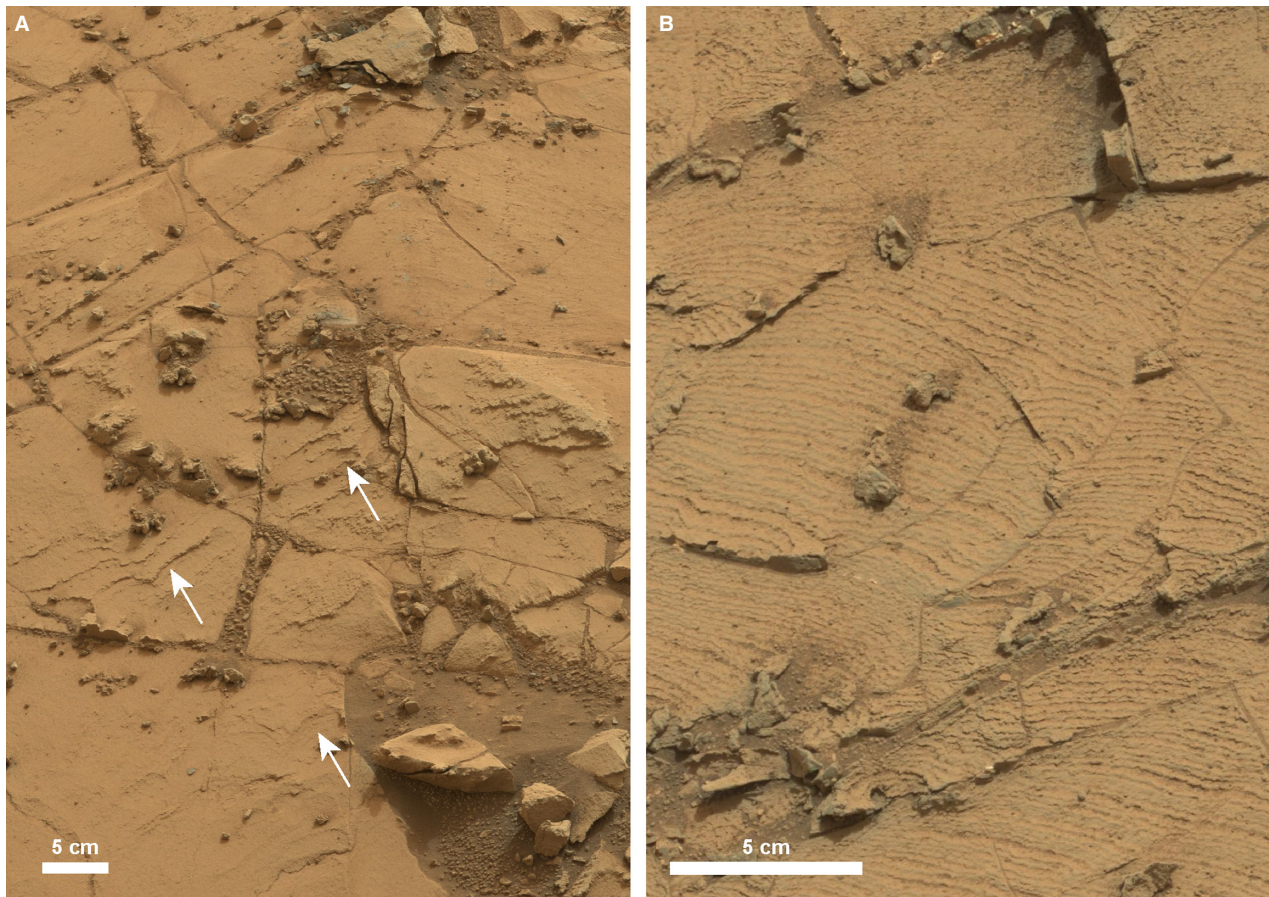


Fig. 5. Sub-facies of the thinly laminated mudstone facies. (A) Discontinuous, unevenly laminated sub-facies exposed at Pink Cliffs acquired with the Mastcam M-100 camera on Sol 810. (B) Rhythmically laminated sub-facies exposed at the Calico Mountain area near Telegraph Peak acquired with the Mastcam M-100 camera on Sol 837.

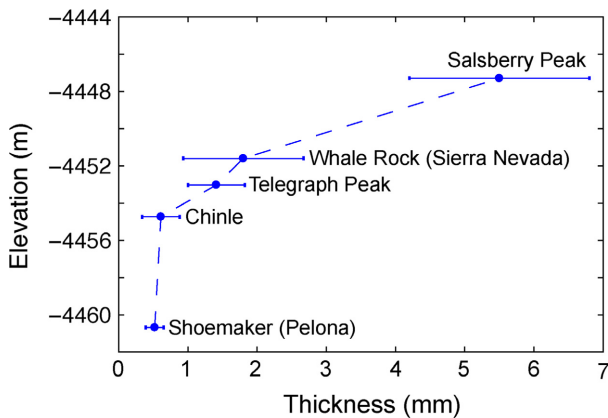


Fig. 6. Elevation versus lamination thickness for five areas measured within Pahrump Hills. Solid points represent mean values; error bars in x represent one standard deviation.

have not been positively identified in this facies. Individual laminae are on the order of several

millimetres thick. Thicknesses measured for 60 laminae discernible in a Mastcam right-eye image mosaic with *ca* 1 mm pixel⁻¹ image resolution range from 3.3 to 9.2 mm and exhibit an average thickness of 5.5 mm (Salsberry Peak target, Figs 6 and S3-1, Table S3-1). Because the M-100 images were the only image data available to measure laminations of this facies, laminations on the order of the thinnest laminations measured elsewhere at Pahrump Hills were not resolvable. Laminae can be traced laterally over length scales of tens of centimetres, although tracing laminations to greater distances is made challenging by the irregular, blocky nature of the outcrop and the presence of cross-cutting veins and fractures.

Cross-stratified sandstone

The cross-stratified sandstone facies contains white, tan and grey-coloured coarse silt to coarse sand-sized grains that make up at least *ca* 30%

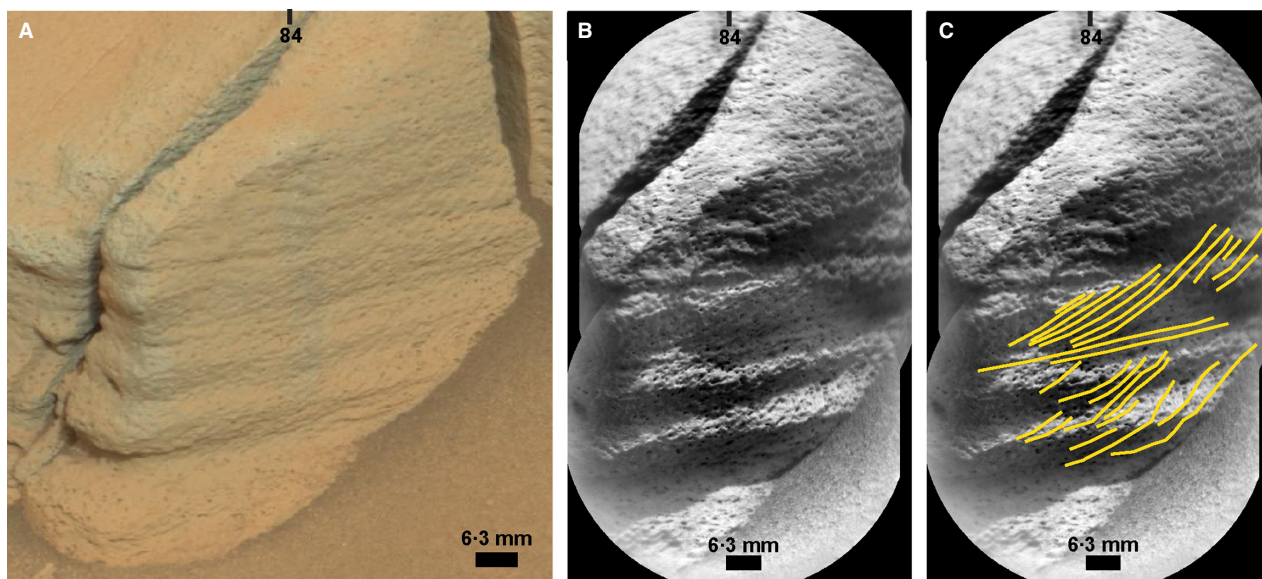


Fig. 7. Possible ripple cross-lamination observed in Book Cliffs in: (A) Mastcam M-100 mosaic acquired on Sol 813, (B) ChemCam RMI image mosaic of the Goblin Valley target, unannotated, (C) ChemCam RMI image mosaic of the Goblin Valley target, annotated to show possible ripple cross-lamination sets separated by planar laminations.

of the exposed rock surface area (Fig. 14). One hundred and twenty-nine individual grains measured in a MAHLI image of a dust-free, unbrushed surface within Whale Rock range in diameter from *ca* 50 to 900 μm (coarse silt to coarse sand) with an average grain size of 240 μm (fine sand; Fig. S2-2, Table S2-2). The remainder of the exposed surface area is dark grey matrix in which individual grains generally cannot be resolved, suggesting a predominant grain size of very fine sand or finer. Discernible grains within this facies are matrix-supported, sub-rounded to rounded, well-sorted, and exhibit moderately low to high sphericity (Fig. 14). Grains appear randomly oriented and no obvious grading is observed within individual laminae. Laminae thickness is sub-millimetre to millimetre-scale. Measurement of 34 laminae reveals a thickness range of 0.3 to 4.5 mm with an average individual lamina thickness of 1.8 mm (Figs 6 and S3-1, Table S3-1). Sedimentary structures observed within this facies include stacked sets of ripple-scale and dune-scale cross-stratification (Figs 15 and 16), including subcritically climbing ripples and dunes bounded by low angle bounding surfaces (Figs 15C, 15D and 16B). Cross-stratified beds range in thickness from *ca* 2 to 10 cm (Fig. 15). Individual foresets dip predominantly to the south-east, are tangential to basal truncation surfaces, and sometimes form wedges that thin down-dip (Fig. 16A). Foreset laminations

are sometimes observed to exhibit very even, regular thicknesses (Fig. 16B). Climbing ripples whose crest heights are <1 cm and whose angle of climb is *ca* 40° also occur (Fig. 16B).

SEDIMENTARY SUCCESSION AT PAHRUMP HILLS

The sedimentary succession at Pahrump Hills is illustrated in Fig. 17. The base of Pahrump Hills is composed of thinly laminated mudstone, with both the Confidence Hills and Shoemaker areas exhibiting geometrically discordant laminae of the rhythmic subfacies (Fig. 8). Thinly laminated mudstone in the vicinity of Pink Cliffs (−4459.5 m) is the best example of the uneven, discontinuously laminated subfacies exposed at Pahrump Hills (Fig. 5A). About 3 m above the base of the section (−4458 m), the Book Cliffs area exhibits parallel laminations of the thinly laminated mudstone facies, but with abundant distinguishable silt to very fine sand grains (i.e. Fig. 4D). Book Cliffs is also the only area composed of thinly laminated mudstone that exhibits possible ripple cross-lamination (Fig. 7). An interval of thinly laminated mudstone approximately 1 m thick (−4457.5 to −4456.5 m) separates the Book Cliffs area from the erosion-resistant ridges exposed in the Alexander Hills area (−4456 m). The thinly laminated mudstone

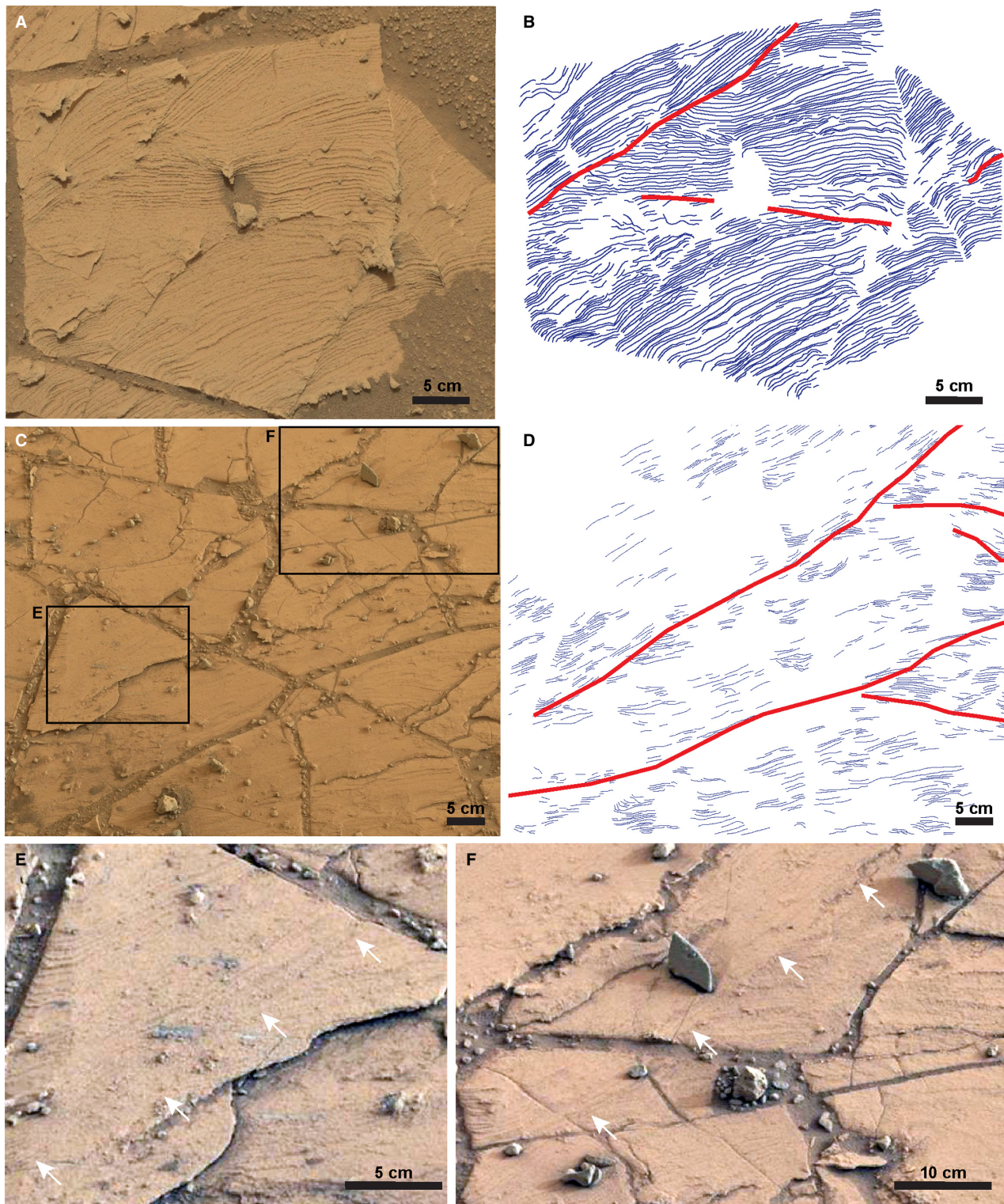


Fig. 8. Geometric discordances within the thinly laminated mudstone facies: (A) Mastcam M-34 mosaic acquired on Sol 797 midway through the rover's traverse from Whale Rock to the base of the section at an elevation approximately equivalent to Alexander Hills; with (B) annotated laminae and truncation surfaces. (C) Confidence Hills imaged by Mastcam M-34 on Sol 803; and (D) annotated laminae and truncation surfaces. (E) and (F) Show example truncations surfaces within the mosaic in (C), whose tone, contrast and colour has been enhanced to highlight laminations.

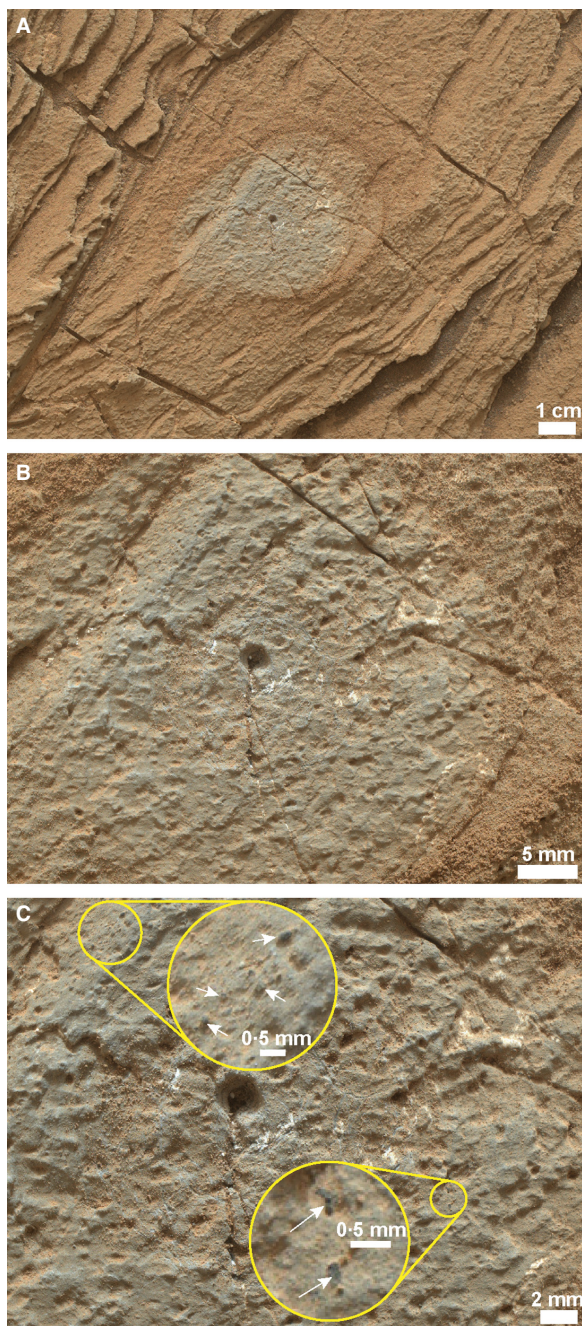


Fig. 9. Mars Hand Lens Imager (MAHLI) images of the low-angle cross-stratified mudstone at the Goldstone target at Chinle taken at successively decreasing working distances: (A) MAHLI image (0830MH000190001 0301787C00) acquired at a working distance of 26.5 cm showing the brushed bedrock spot and through-going laminations, (B) MAHLI z-stack (0831MH00017000003 01834R00) acquired a working distance of 6.9 cm showing a close-up view of the brushed spot, (C) MAHLI z-stack (0831MH0001700000301832R00) acquired at a working distance of 3.8 cm. Arrows indicate the location of discernible silt to very fine sand-sized grains.

between Book Cliffs and Alexander Hills consists of geometrically discordant laminae of highly even and regular thickness and is a prime example of the rhythmic subfacies (Fig. 5B). The ridges at Alexander Hills are composed of the rhythmic subfacies of the thinly laminated mudstone. Differential cementation due to secondary diagenesis rather than a change in primary grain size or lamination style probably best explains the variation in outcrop expression throughout this interval, since no noticeable change in grain size was observed in the erosion-resistant ridges versus recessively-weathering bedrock.

A *ca* 1 m thick interval of the rhythmic subfacies of the thinly laminated mudstone (fig. 7b of Grotzinger *et al.*, 2015) occurs above Alexander Hills (–4456 m to –4455 m). At –4455 m, a sharp, irregular contact varying a few tens of centimetres in elevation occurs between thinly laminated mudstone and a broad, shallow lens consisting predominantly of low-angle cross-stratified mudstone (Fig. 18A and B). This lens, whose eastern and western ends are referred to as Gilbert Peak and Chinle, respectively, extends *ca* 20 m from east to west and is *ca* 70 cm thick at its centre (30 : 1 aspect ratio). The upper contact of the lens is gradational into overlying thinly laminated mudstone. At the Chinle area, sets of low-angle cross-stratified mudstone pass upward into climbing ripple lamination of the cross-stratified sandstone facies (Fig. 18C and D). The interval of thinly laminated mudstone (–4454.5 to –4452 m) that overlies Chinle and Gilbert Peak is composed of rhythmic thinly laminated mudstone.

Cross-stratified sandstone also occurs in two discrete lenses named Newspaper Rock and Whale Rock which are located in the upper half of the Pahrump Hills section (–4454 m and –4452 m, respectively; Fig. 18). The Whale Rock lens is *ca* 8 m in length, reaches a maximum thickness of *ca* 1.5 m (*ca* 5 : 1 aspect ratio), and tapers to the north-west and south-east. The Newspaper Rock lens measures *ca* 30 to 40 cm at its thickest and is *ca* 6 m in length (15 : 1 aspect ratio, Fig. 18D). The two lenses are separated laterally by *ca* 10 m, with the Whale Rock lens occurring *ca* 2 m higher in the section than the Newspaper Rock lens (Fig. 18A). The basal contact of the Newspaper Rock lens (Fig. 18D) is largely obscured by sand, but at Whale Rock the basal contact is sharp and overlies thinly laminated mudstone (Fig. 18E). The upper contacts of Whale Rock and Newspaper Rock are both gradational with overlying thinly laminated mudstone.

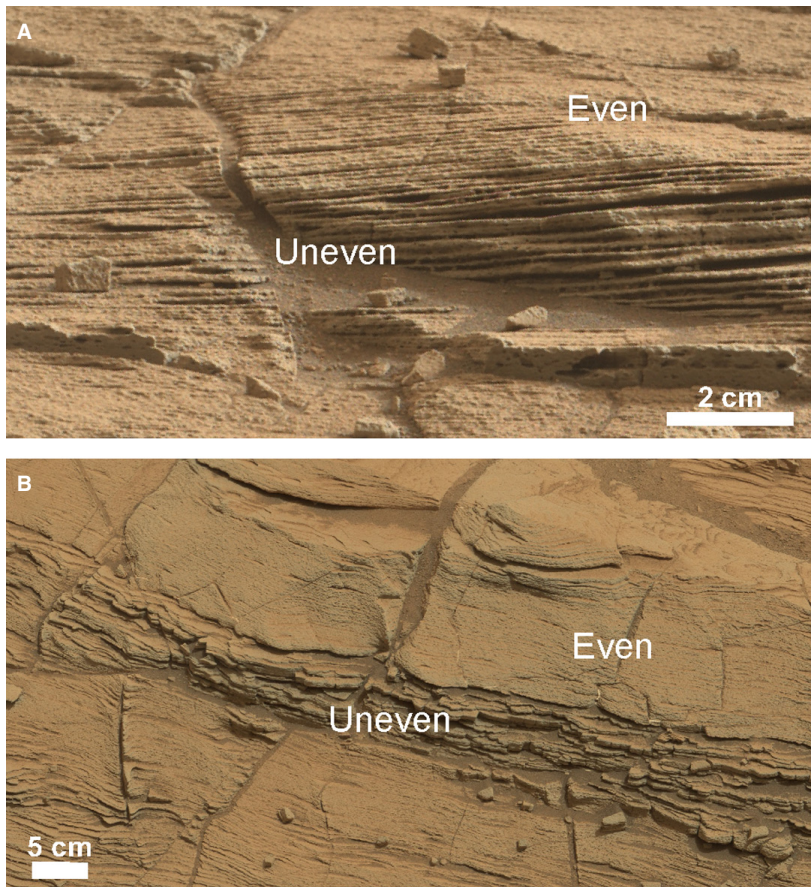


Fig. 10. Variable lamination characteristics observed within the low-angle cross-stratified mudstone at Chinle. (A) Laminated intervals exhibiting extremely regular and even thickness underlain by an interval of laminations exhibiting uneven thickness observed in an oblique MAHLI image (0828MH0004540000301740R00). (B) Laminations of very even, uniform expression and uneven thickness observed in a Mastcam M-100 mosaic acquired on Sol 792.

Approximately 3.5 m of thinly laminated mudstone is inferred to be present above Whale Rock (–4451 to –4448 m), although this interval was not examined in detail because the steepness of the outcrop and abundance of angular pebbles and cobbles precluded safe traverse of the rover. Mastcam images show this recessive interval to grade up-section from predominantly mudstone to the thickly laminated mudstone–sandstone exposed at Salsberry Peak, an outcrop whose base is located at –4448.5 m. Salsberry Peak forms a 1.5 to 2.0 m thick caprock at the top of the Pahrump Hills section (Fig. 13).

DEPOSITIONAL PROCESSES AND ENVIRONMENTS RECORDED WITHIN THE PAHRUMP HILLS MEMBER

Depositional interpretation for the thinly laminated mudstone

A depositional model for the Pahrump Hills member must account for the occurrence of a nearly 13 m thick section of continuously

exposed, uniform, sub-millimetre to millimetre-scale parallel laminated mudstone. Processes considered for the deposition of the thinly laminated mudstone facies include: aeolian traction deposition, suspension settling of dust or ash from the atmosphere, suspension settling through a water column and deposition by currents in a subaqueous setting.

Thin planar laminations of uniform thickness are characteristic of some types of aeolian strata, with the uniformity of laminae resulting from the consistency of wind velocity and deposition rate in a given area over time (Hunter, 1977). The aeolian stratification types that might best fit the lamination style observed at Pahrump Hills include plane bed lamination or subcritically climbing translational strata (Hunter, 1977, 1981). Plane bed lamination, formed when winds are strong enough to suppress ripple formation, is relatively rare in modern and ancient aeolian deposits on Earth (Hunter, 1977, 1981). The conditions needed to suppress aeolian ripple formation might be even less likely to occur on Mars if the atmospheric pressure at the time of Pahrump Hills member deposition was as low

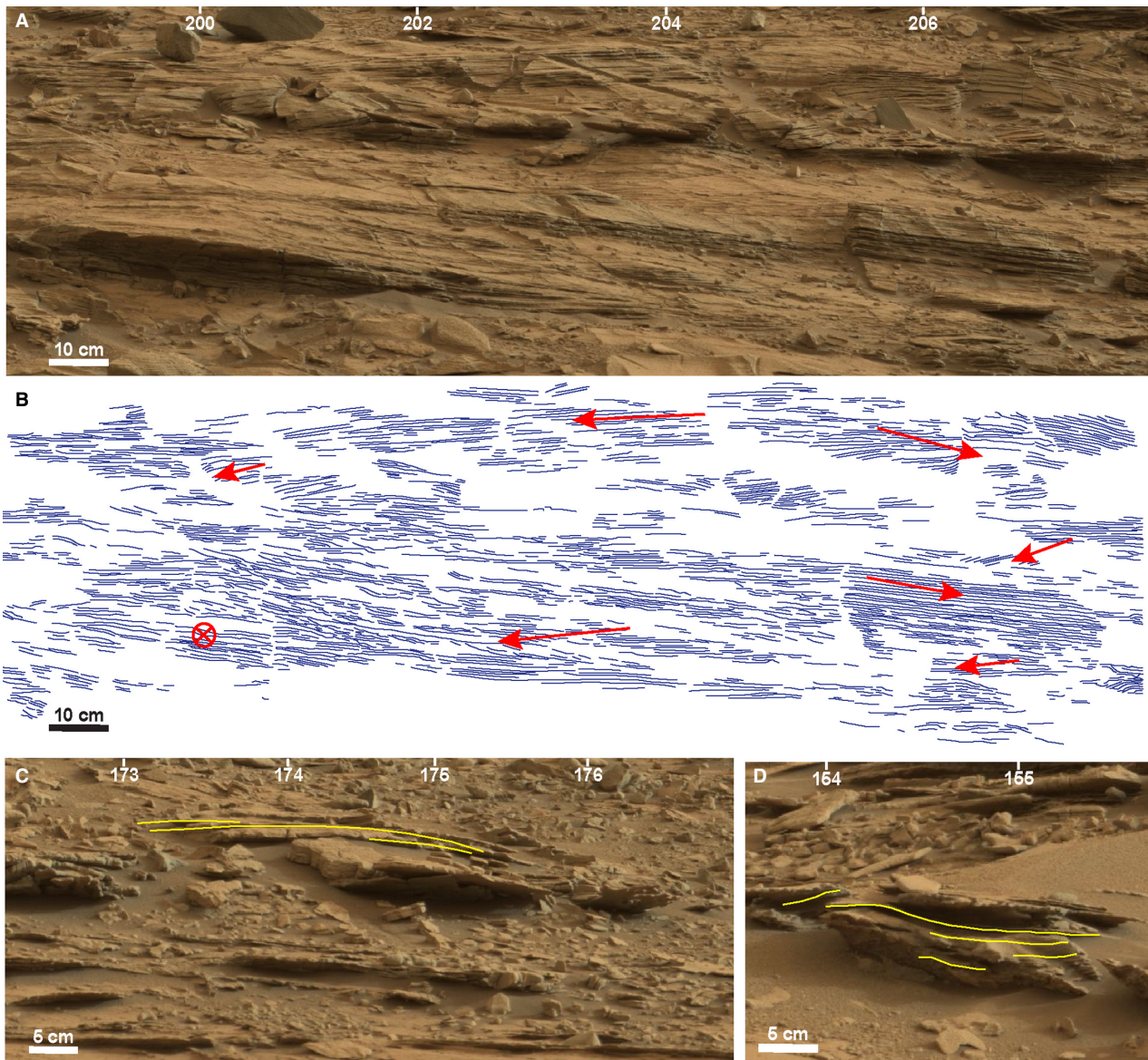


Fig. 11. Variably dipping laminations observed at the Chinle area in a Mastcam M-100 mosaic acquired on Sol 821: (A) unannotated Mastcam; and (B) lamination traces. Arrows indicate apparent dip direction; circle with the cross indicates an apparent dip direction into the page. (C) and (D) Show variable dipping convex to concave laminae geometries.

as that of present-day Gale crater (7 to 11 millibars; Martínez *et al.*, 2017). Furthermore, sets of aeolian plane bed laminations are typically thin and often indistinctly defined when observed on Earth, rarely exceeding *ca* 0.5 to 1.0 m in thickness before transitioning into other types of aeolian stratification (Hunter, 1977, 1981). Given the thickness and lateral extent of the thinly laminated mudstone facies at Pahrump Hills, as well as the distinctness of laminae observed there, an origin as aeolian plane bed deposits seems unlikely.

Subcritically climbing wind ripple lamination is a more plausible aeolian interpretation for the thinly laminated facies. Wind ripple stratification is very commonly observed in modern and ancient aeolian systems on Earth, and several known outcrops on Earth up to 7 m thick are composed almost entirely of low-angle to flat climbing wind ripple strata, for example Hunter (1981) and Clemmenson & Hegner (1991). A wind ripple stratification interpretation for the thinly laminated mudstone facies at Pahrump Hills would be particularly compelling if ripple-foreset

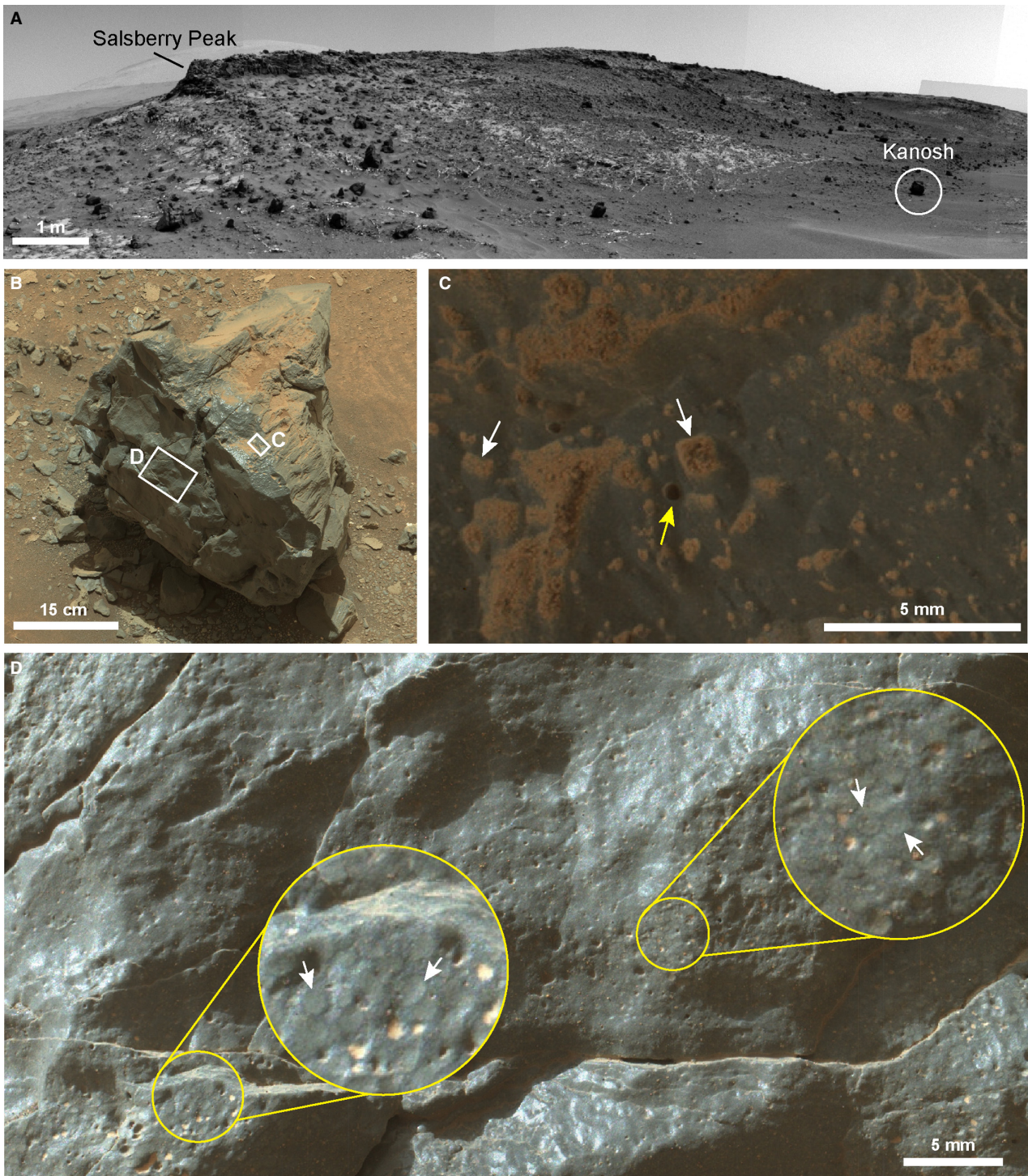


Fig. 12. (A) Navcam mosaic showing the location of the Kanosh cobble relative to the Salsberry Peak outcrop and nearby field of boulders and cobbles. (B) Mastcam M-100 mosaic of the Kanosh cobble shed from the Salsberry Peak outcrop acquired on Sol 940. (C) Circular (yellow arrow) and dust-filled rectangular pits (white arrows) observed in a MAHLI image 0942MH0001630000303660R00 of the Little Devil target. (D) Rounded grains observed in the Devils Punchbowl MAHLI target (0942MH0001630000303664R00).

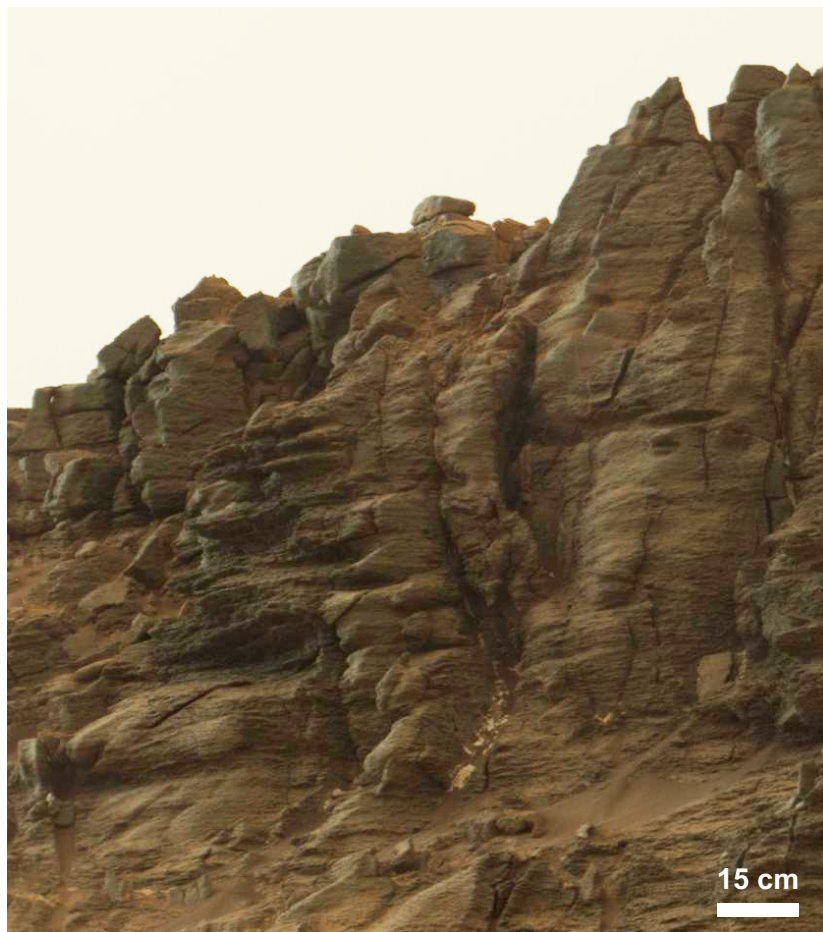


Fig. 13. Laminations within Salsberry Peak observed in Mastcam M-100 mosaic acquired on Sol 855.

cross-lamination, inverse grain-size grading, preserved ripple forms, or a transition into aeolian cross-beds had been observed throughout the outcrop. Yet evidence for such features is largely absent at Pahrump Hills, with only one instance of possible ripple-foreset cross-lamination observed at Book Cliffs. As also noted by Grotzinger *et al.* (2015), there is no evidence that the thinly laminated mudstone at Pahrump Hills is interbedded with or grades into aeolian cross-bedded strata. A subcritical climbing wind ripple interpretation cannot be entirely precluded based on the absence of evidence for features typically observed in aeolian settings and given resolution limits that preclude observation of characteristics like inverse grading, but this interpretation is less convincing as a result.

Another possible explanation for the thin, uniform laminations at Pahrump Hills is suspension settling of wind-blown dust, silt or distal volcanic tephra from the atmosphere. Grotzinger *et al.* (2015) rejected this interpretation based on the observations that, on Earth, volcanic tephra and aeolian loess deposits are generally

massively bedded unless fragments or particles have fallen through a water column in which increased fluid drag and variable settling velocities enable effective grain-size sorting and lamina formation. Siebach *et al.* (2017) showed that the composition of the Pahrump Hills member does not match that of Mars dust, suggesting that an origin as a duststone is unlikely. This study finds no additional evidence to support an interpretation that the thinly laminated mudstone was deposited by suspension settling from the atmosphere.

A third process considered to explain the uniformity and thinness of laminations observed throughout the Pahrump Hills mudstone succession is suspension settling through a water column in a low-energy setting. Metres-thick fine-grained laminated rhythmites have been observed in overbank levée and splay deposits on Earth (e.g. Farrell, 1987) but an overbank interpretation for Pahrump Hills seems unlikely given that thick, very fine-grained overbank suspension deposits are exceedingly rare in pre-vegetated fluvial systems preserved in the rock

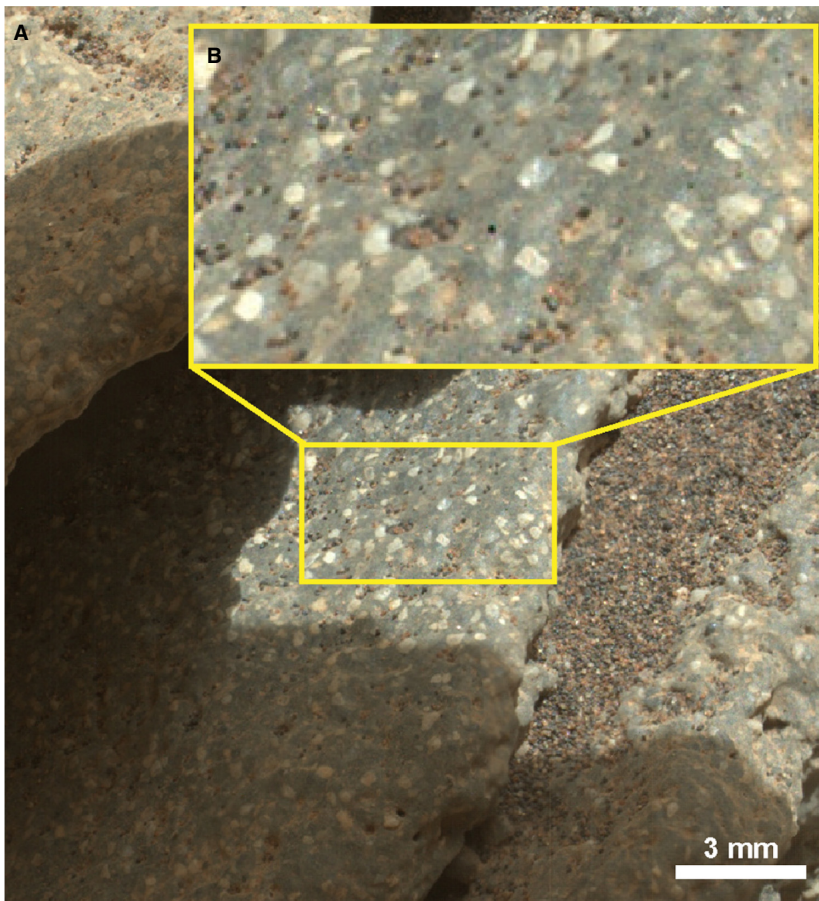


Fig. 14. (A) Light-toned white and tan grains present in the Sierra Nevada target at Whale Rock (MAHLI image 0860MH0004580000302120R00). (B) Inset showing close-up view of light grains in a dark grey very fine-grained matrix.

record on Earth (Davies & Gibling, 2010; Long, 2011; Gibling *et al.*, 2014; McMahon & Davies, 2018). Furthermore, there is no evidence for sub-aerial exposure within the section at Pahrump Hills (for example, reworking by wind, pebble lags and desiccation cracks), nor for point bar deposits or stacked channel deposits that would probably be associated with overbank deposits of the thickness of the Pahrump Hills mudstone. Rather, observations presented here for the very fine grain size, lamination thickness and general lack of bedforms indicative of traction transport within the thinly laminated mudstone facies are most consistent with deposition in a subaqueous lacustrine setting.

Continuous, thin laminations of uniform thickness are commonly found as varves in proglacial and periglacial lakes on Earth that experience repeated seasonal changes that affect the grain size, composition and sorting of sediments entering the lake (Smiley, 1955; Anderson & Dean, 1988). Cyclic forcing or modulation within the fluvio-lacustrine system on a number of different timescales, including daily or annual changes in temperature and river flow, could have been

responsible for the formation of uniform, thin laminations at Pahrump Hills. Although varves have been interpreted by some to result predominantly from suspension settling from hypopycnal plumes (overflows) entering lakes (e.g. Antevs, 1951), bottom-hugging turbidity currents are also thought to be an important depositional mechanism in varve formation (e.g. Sturm & Matter, 1978; Anderson & Dean, 1988). The occurrence of low-angle truncation surfaces observed throughout the thinly laminated mudstone facies (Figs 8 and 17) suggests a depositional process in addition to passive settling from suspension. Truncation surfaces are distinct in that they are invariably overlain by laminae that are conformable with the underlying truncation surface itself with no observed lateral changes in laminae thickness (Fig. 8A). They most closely resemble subaqueous 'scour and drape' structures (Dott & Bourgeois, 1982; Duke *et al.*, 1992; Cheel & Leckie, 1993; de Luca & Basilici, 2013) which form when scouring of deposited sediment by wave or current action is followed by deposition of sediment settling through the water column to form beds or laminae that drape the original

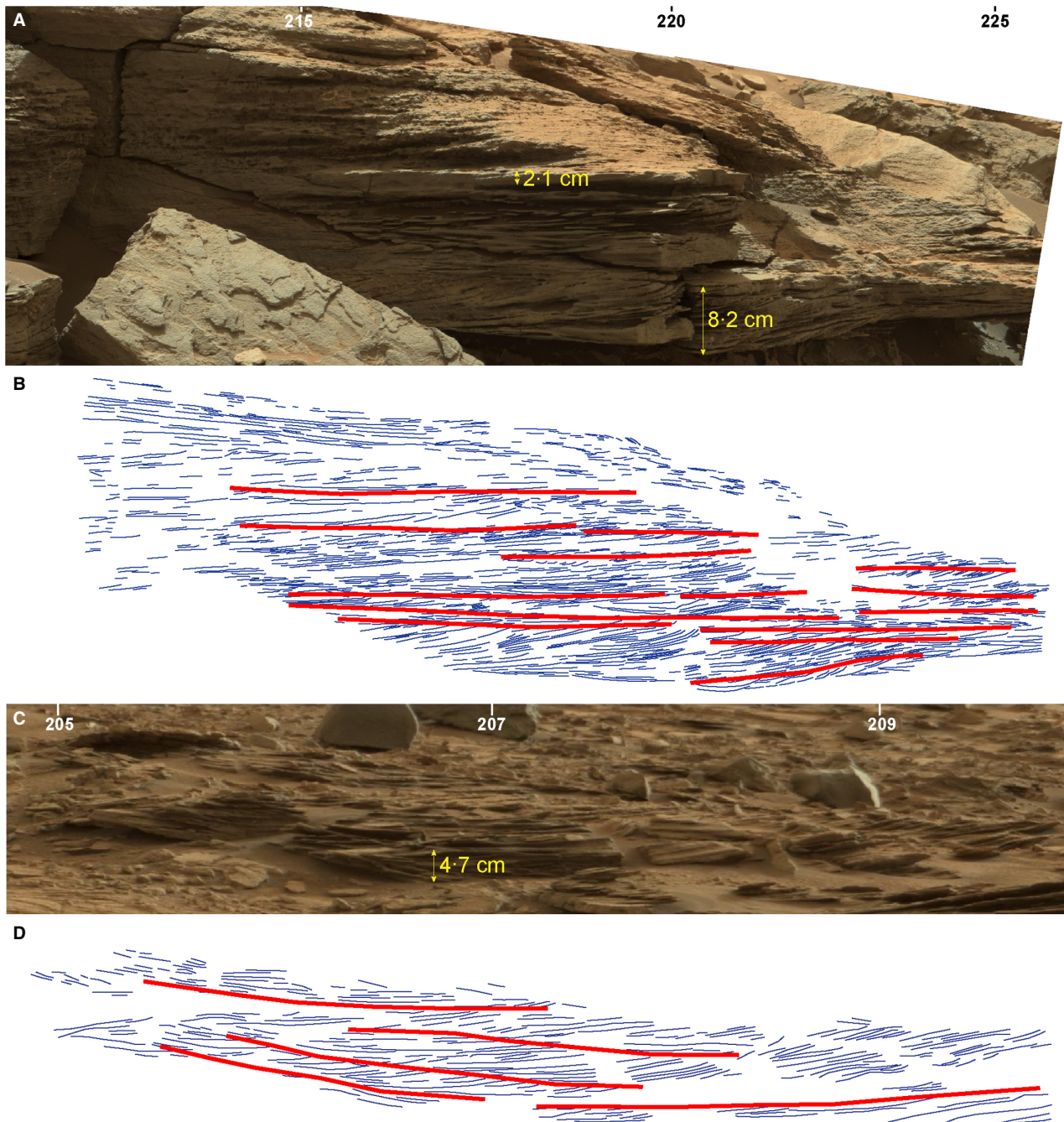


Fig. 15. Dune and ripple-scale cross-stratification observed in a Mastcam M-100 mosaic acquired on Sol 821 at: (A) and (B) Whale Rock, and (C) and (D) subcritically climbing dune and ripple-scale cross-stratification in the upper portion of Chinle. Bounding surfaces between sets are annotated in red

scour without the influence of currents or waves. The absence of evidence for wave action, for example symmetrical bedforms or hummocky cross-stratification, throughout the thinly laminated mudstone facies favours deposition of the scour and drape structures by current action.

In the context of a subaqueous lacustrine setting, the occurrence of scour and drape

structures in the Pahrump Hills member further constrains the depositional origin of the thinly laminated mudstone facies. Grotzinger *et al.* (2015) proposed deposition from either hyperpycnal or hypopycnal plumes as possible interpretations for the thinly laminated mudstone facies. The presence of abundant scour and drape structures probably rules out deposition solely

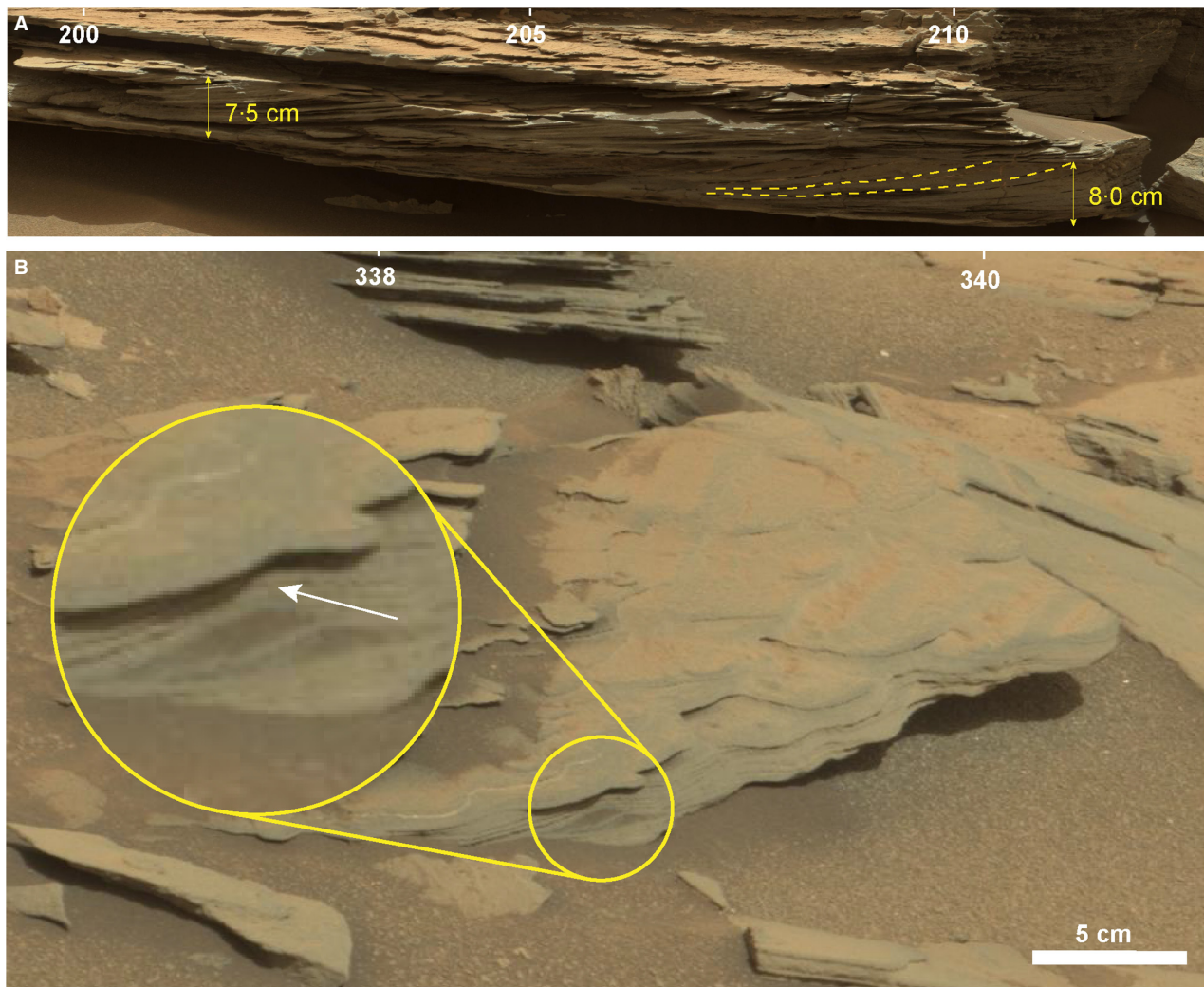


Fig. 16. (A) Dune foresets at Whale Rock observed in a Mastcam M-100 mosaic acquired on Sol 862; tangential foresets thin towards the base. (B) Critically climbing ripples at Newspaper Rock in a Mastcam M-100 mosaic from Sol 921.

by hypopycnal plumes, which would only be expected to passively rain out sediment. By contrast, bottom-hugging turbidity currents can originate from plunging river plumes, i.e. hyperpycnal flows (Mulder & Syvitski, 1995; Mulder *et al.*, 2003) or wave-generated resuspension. As noted by Grotzinger *et al.* (2015), the section at Pahrump Hills does not show evidence for coarser graded beds and is largely lacking in bedforms characteristic of flow deceleration sequences that would be expected from failure of a sandy clinof orm fed by a coarse-grained braided river.

In modern and ancient deposits associated with plunging river plumes on Earth, thick deposits of parallel laminated fine-grained

sediments are common and characteristic (Mutti *et al.*, 1996; Myrow *et al.*, 2008; Lamb *et al.*, 2008; Bhattacharya & MacEachern, 2009; Olariu *et al.*, 2010; Zavala *et al.*, 2011). Internal scour surfaces (Zavala *et al.*, 2006; Bhattacharya & MacEachern, 2009) and low-angle laminations (Zavala *et al.*, 2006; Lamb *et al.*, 2008; Zavala *et al.*, 2011) occur in facies associated with the collapse and lofting of a plume's suspended load and are particularly common in shallow water systems (Zavala *et al.*, 2011). Although the presence of traction transport bedforms is often an important indicator of the waxing and waning of flows characteristic of plunging plume deposition (Mulder *et al.*, 2003), planar laminated mudstones and siltstones lacking evidence for

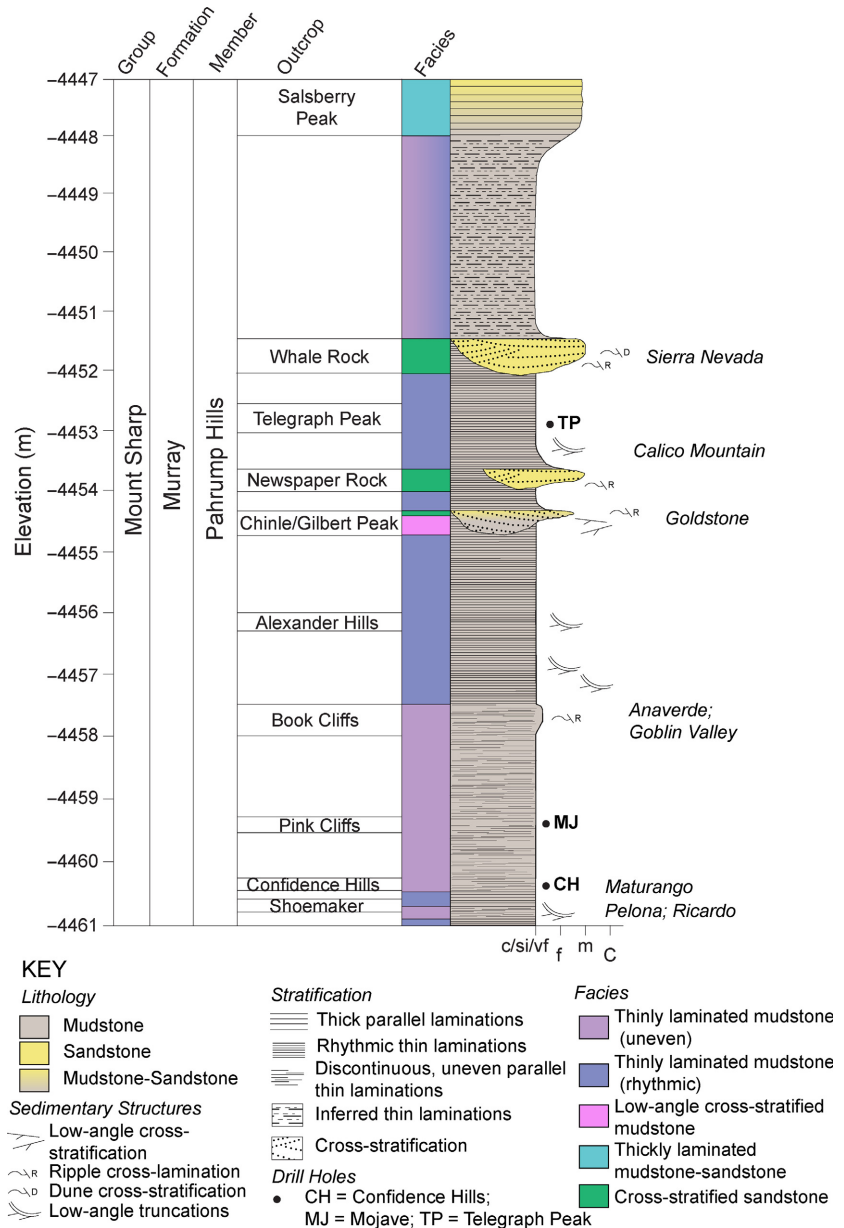


Fig. 17. Stratigraphic column for the Pahrump Hills succession. Grain size is abbreviated as: c = clay; si = silt; vf = very fine sand; f = fine sand; m = medium sand; C = coarse sand.

traction transport are commonly observed in the distal reaches of hyperpycnal systems where deposition of the finest-grained material occurs either by lofting by the hyperpycnal plume and subsequent settling from the water column (Zavala *et al.*, 2011, and sources within) or via passive settling between flow events.

Similarities between the thinly laminated mudstone facies and distal plunging plume deposits recognized on Earth, coupled with the common occurrence of scour and drape structures throughout the Pahrump Hills section, favour an origin for the bottom currents as muddy hyperpycnal river plumes. In this

depositional context, the mudstone laminations, which range from 0.2 to *ca* 10 mm in thickness and average *ca* 2 mm overall (Fig. 6), are interpreted to represent deposition primarily by plunging plumes (Mulder *et al.*, 2003; Lamb *et al.*, 2008). Although it is unlikely that every single lamination within the thinly laminated mudstone facies represents an individual event bed, a significant proportion of the laminae at Pahrump Hills may represent event beds. Given the total thickness of this facies (*ca* 11 m) and an average laminae thickness of *ca* 2 mm, there could be as many as thousands of event beds recorded in the Pahrump Hills succession.

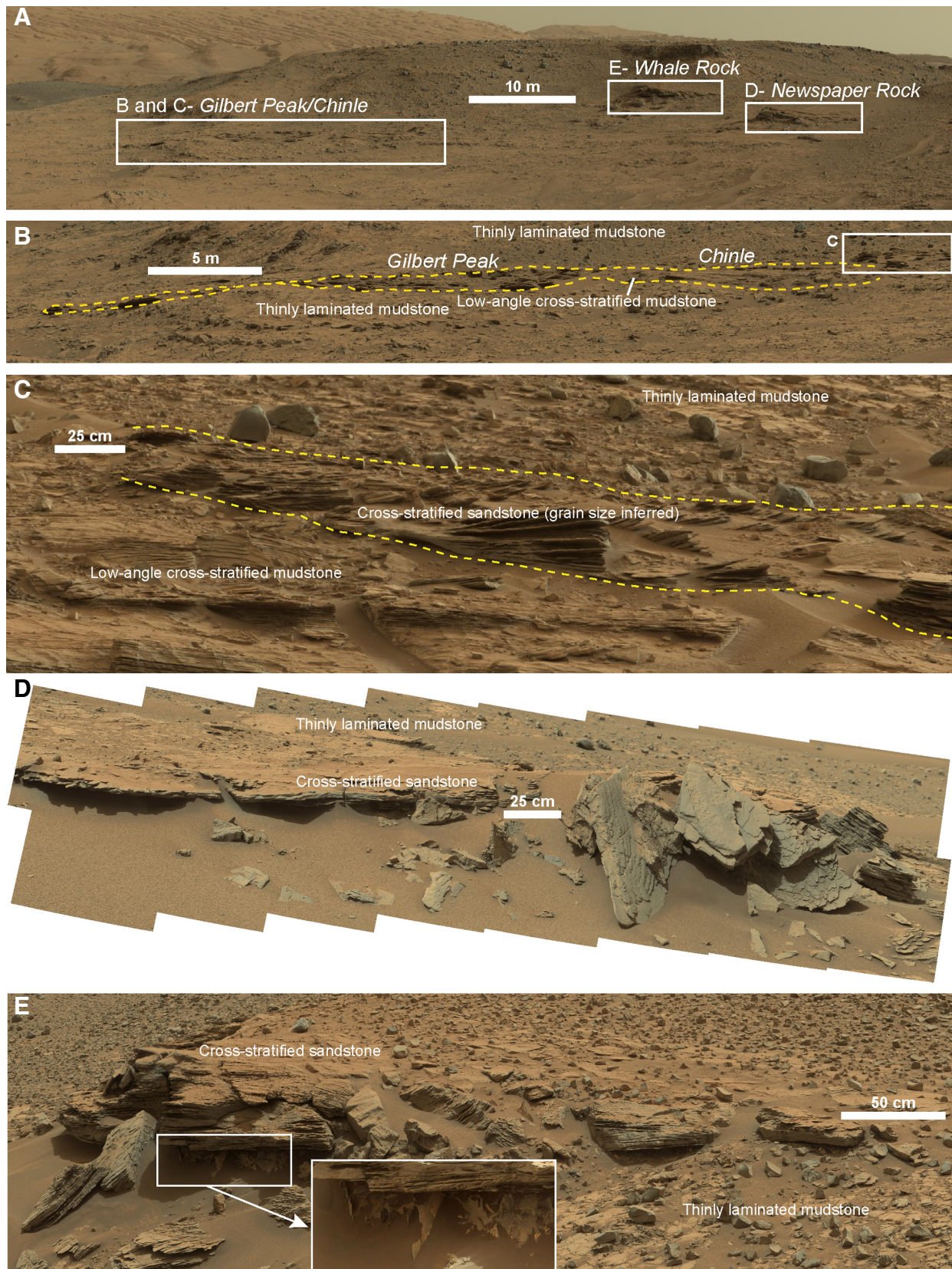


Fig. 18. (A) Cross-stratified mudstone and sandstone lenses at Pahrump Hills annotated in a Mastcam M-100 mosaic from Sol 751; (B) and (C) Gilbert Peak/Chinle (Mastcam M-100 mosaic acquired on Sol 821). (D) Newspaper Rock (Mastcam-100 mosaic acquired on Sol 903). (E) Whale Rock (Mastcam M-100 mosaic acquired on Sol 837).

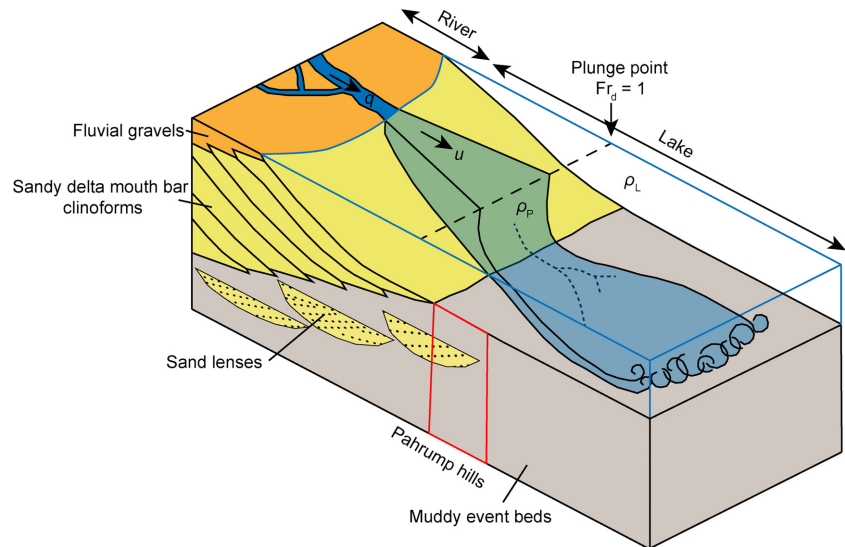


Fig. 19. Schematic illustrating the conceptual model for the deposition of the Pahrump Hills member mudstone and sandstone lenses via river-fed plunging plumes in an ancient Gale crater lake. Proximal sand lenses form from the incision of subaqueous channels (dashed lines within the plume) when the plume plunges.

Depositional interpretation for the low-angle cross-stratified mudstone and cross-stratified sandstone facies

Grotzinger *et al.* (2015) proposed two possible interpretations for the depositional origin of the coarse-grained cross-stratified lenses observed at Pahrump Hills: (i) subaqueous channelized delta foreslope deposits deposited under decelerating flow conditions after an initial phase of scour; or (ii) fluvial deposits that were incised into lacustrine deposits during lake level drawdown. Observations presented in the current study support the former interpretation. Given the absence of mudcracks and the paucity of coarser grained sandstones and gravels throughout the section, it seems unlikely that the Pahrump Hills member records evidence of substantial lake drying that would be expected if the Whale Rock–Newspaper Rock–Chinle lenses are regarded as subaerial fluvial deposits. Furthermore, the sandstones and conglomerates of the Bradbury group (Williams *et al.*, 2013; Vasavada *et al.*, 2014; Grotzinger *et al.*, 2015; Stack *et al.*, 2016; Rice *et al.*, 2017), the most plausible analogue for the river systems that fed the Gale crater lake (Grotzinger *et al.*, 2015), probably were deposited as wide sheets of coarse alluvium exhibiting width to thickness ratios greater than 1000 : 1, typical of a braided fluvial fan (Gibling, 2006). In contrast, sandy lenses cut into the Pahrump Hills mudstone have widths that are too narrow compared to their thickness (aspect ratios range from 5 : 1 to *ca* 30 : 1) to represent alluvial braid plain channels.

The sandstone facies exposed at Chinle/Gilbert Peak, Whale Rock and Newspaper Rock

are most consistent with an interpretation in which each lens represents the incision of a sublacustrine channel followed by deposition during a short-lived, energetic plunging plume event. The occurrence of these three sandstone lenses at different stratigraphic heights within the Pahrump Hills succession suggests that each lens represents a distinct plume event. The upward transition from low-angle cross-stratified mudstone to dune and ripple cross-laminated sandstone in the upper part of the Chinle outcrop is consistent with variations in the flow velocity (Mulder & Alexander, 2001; Sumner *et al.*, 2008; Zavala *et al.*, 2011). The presence of variably dipping, convex laminations within Chinle and Gilbert Peak could represent cross-sections through bar deposits within a shallow, broad channel or Froude-supercritical bedforms such as antidunes or cyclic steps (Kostic & Parker, 2006; Kostic, 2011; Cartigny *et al.*, 2011; Postma *et al.*, 2014). Cross-laminated sets observed at Whale Rock and Newspaper Rock could also be consistent with bedforms such as migrating scour and fill structures formed during Froude supercritical flows (e.g. Cartigny *et al.*, 2014). Froude-supercritical bedforms would be consistent with plunging plumes, which have Froude numbers near one (Lee & Yu, 1997; Lamb *et al.*, 2010). Palaeocurrent directions inferred from the southward dip of climbing ripple foresets within Whale Rock suggest a predominantly southward sediment transport direction, consistent with sediment transport and progradation of a river system from the northern rim of Gale crater towards the centre of the crater basin.

DEPOSITIONAL MODEL FOR PAHRUMP HILLS

Observations of sedimentary structures, textures and grain size presented here support a depositional model for the Pahrump Hills member in which southward-flowing river-fed plunging plumes deposited event beds in a lacustrine setting (Fig. 19). As braided rivers flowed south into a lake within Gale crater, sediment-laden plumes plunged near the toes of delta mouth bar clinoforms (Grotzinger *et al.*, 2015), scouring previously deposited sediments. Such a process would have deposited the coarser sandstone lenses observed in the upper half of the Pahrump Hills section. Suspension settling through the water column following plume lofting or via passive fallout between plume events deposited the draping laminations of the scour and drape structures observed throughout the thinly laminated mudstones at Pahrump Hills. Deposition recorded within the thinly laminated mudstone in the lower half of the Pahrump Hills section must have occurred at a position distal enough from the lake margin such that deposition was dominated by suspension settling and/or lofting of fines towards the end of each plunging plume event, but shallow enough to record evidence for scouring earlier in the event to form the observed scour and drape structures. Such conditions could be achieved at the distal ends of subaqueous plume lobes or at plume margins (Zavala *et al.*, 2011).

As the river system prograded basinward either via delta progradation or lakeward shift of the river mouth, successive channelized flows including the proximal mudstone and sandstone lenses at Chinle, Newspaper Rock and Whale Rock were deposited near the plunge point. A slight backstep of the system, or channel switching could explain the return to thinly laminated mudstone above Whale Rock, but continuing progradation resulted in a transition from the thinly laminated mudstone to thickly laminated mudstone and sandstone higher up in the succession observed at Salsberry Peak.

The overall thickening-upward trend observed in the lamination measurements from the Pahrump Hills succession (Fig. 6) supports a progradational model for the river system into the basin. The trend reported here is consistent with the thickening trend reported by Grotzinger *et al.* (2015) and seen in the Hurowitz *et al.* (2017) thickness measurements between the Alexander

Hills, Chinle and Telegraph Peak areas of Pahrump Hills. The thickening-upward trend observed at Pahrump Hills is likely to be the result of a transition up-section to a more proximal, shallower water environment created as the river system prograded out into the basin. Proximal to the basin margin, plunging plumes would be expected to have increased sediment load and would have deposited coarser, thicker laminae. As the plumes extended further into the basin, they would thin, become more dispersed, and lose flow competency resulting in the deposition of increasingly thinner laminae with distance from the lake margin. The occurrence of coarser-grained lenses exhibiting sedimentary structures characteristic of traction transport in the upper half of the Pahrump Hills section, coupled with the transition into coarser-grained thickly laminated mudstone–sandstone suggests that the Pahrump Hills member records a progradational succession in which the distal lacustrine setting preserved at the base of the section transitions up-section to a more proximal basin margin environment (Fig. 19).

PLUNGING PLUME ANALYSIS

The observations here suggest that plunging river plumes may have been the dominant depositional mechanism in the ancient lake recorded at Pahrump Hills. Given the specific conditions under which plunging of a river plume is triggered, this interpretation places important constraints on the salinity of the ancient lake in Gale crater.

Seas and lakes that lack a riverine outlet or significant exchange with groundwater often accumulate solutes, which are delivered by river runoff and left behind and concentrated by evaporation. A global compilation of rivers on Earth (Mulder & Syvitski, 1995) shows that plunging river plumes are relatively uncommon in saline water bodies because saline water is denser than the incoming riverine freshwater, although high suspended sediment concentrations during large floods can sufficiently increase the effective river water density to allow plunging, for example Wright *et al.* (1988). In addition to the necessary condition of a negative buoyancy anomaly for river water, the plume velocity and discharge must also satisfy an instability criteria to trigger plunging (Akiyama & Stefan, 1984; Parker & Toniolo, 2007). Here, two physical constraints on the occurrence of plunging are used to show the

range of sediment concentrations and associated fluid densities within a Gale crater lake.

River plunging occurs at a critical densimetric Froude number, $Fr_d \approx 0.5$ and plumes collapse just beyond the plunge point to $Fr_d \approx 1$ (Lee & Yu, 1997; Lamb *et al.*, 2010). The densimetric Froude number at which plumes collapse should be the same for both Earth and Mars since the transition from potential energy of the plume just prior to collapse to purely kinetic energy upon collapse requires a condition of $Fr_d \approx 1$. The densimetric Froude number, by definition, can be written as:

$$Fr_d^2 = \frac{\rho_L U^3}{(\rho_P - \rho_L) g q} \quad (1)$$

where U is the layer-averaged plume velocity, $g = 3.71 \text{ m}^2 \text{ s}^{-1}$ is the acceleration due to gravity on Mars, q is the volumetric river discharge per unit width, ρ_P is the plume density and ρ_L is the lake density (Fig. 19). To estimate the lake density from Eq. 1, the river discharge, flow velocity near the plunge point and the density of the river plume need to be constrained.

Conglomerates of the Bradbury group are exposed intermittently along the 10 km traverse between Bradbury Landing and the base of Pahrump Hills (Williams *et al.*, 2013; Mangold *et al.*, 2016) and may inter-finger with the Murray formation at Pahrump Hills (Grotzinger *et al.*, 2015). Here, it is assumed that these gravels were deposited by rivers that fed the ancient lake, and the reconstruction estimate of Williams *et al.* (2013) based on gravel transport thresholds is used, which yields a maximum flow depth of 0.9 m and a maximum average flow velocity of 0.75 m s^{-1} , i.e. $q = 0.68 \text{ m}^2 \text{ s}^{-1}$.

To constrain the flow velocity at the plunge point, it is assumed that the sand lenses in the Pahrump Hills member (Chinle/Gilbert Peak, Whale Rock and Newspaper Rock) were deposited near the plunge point. Scour to produce the channel forms and deposition of sands within the lenses both suggest an energetic environment proximal to the plunge point where mouth bar clinofolds create steep topographic slopes and where plunging plumes accelerate due to flow collapse (Fig. 19). The sand lenses within Pahrump Hills contain climbing cross-strata with sets that range in thickness from 2 to 10 cm and critically climbing ripples with crest heights <1 cm, suggesting that the bedforms were near the stability threshold between ripples and dunes. Through an exhaustive compilation of current ripple data on Earth, Lapotre *et al.* (2017) showed that the

stability boundary between ripples and dunes is well-represented by a constant Yalin Number of $\chi = 4$, where the Yalin Number is defined as:

$$\chi \equiv \frac{u_*^2 D^{1/2}}{\nu (Rg)^{1/2}} \quad (2)$$

in which u_* is the bed shear velocity, D is the particle diameter, ν is the kinematic viscosity of water and R is the submerged specific density of sediment. Particle diameter, D is set to 0.24 mm, as observed for Whale Rock, $R = 2.0$ and $\nu = 10^{-6} \text{ m}^2 \text{ s}^{-1}$ for basaltic sand in freshwater. The bed shear velocity can be related to the layer-averaged flow velocity, U , using:

$$U = C_f^{-0.5} u_* \quad (3)$$

where C_f is a bed friction coefficient which is estimated to $C_f \approx 5 \times 10^{-3}$ from (Sequeiros *et al.*, 2010). Using these values with Eq. 2 and $Fr_d \approx 1$ yields an estimate of the flow velocity near the plunge point of $U = 0.38 \text{ m s}^{-1}$. Given these values, depths at the plunge point are predicted to be $q/U = 1.8 \text{ m}$ and plumes tend to collapse to about 70% of that depth after plunging (Lee & Yu, 1997; Lamb *et al.*, 2010), yielding a plume flow thickness of 1.3 m. This hyperpycnal flow thickness is consistent with the sizes of the sand lenses (*ca* 1 m).

Finally, the river plume density can be found from mass balance to be:

$$\rho_P = c\rho_s + (1 - c)\rho_w \quad (4)$$

where c is the depth-averaged, volumetric sediment concentration (dimensionless), $\rho_s = 3000 \text{ kg m}^{-3}$ is the density of basaltic sediment and $\rho_w = 1000 \text{ kg m}^{-3}$ is the density of the river water, assuming freshwater. Suspended sediment loads in coastal rivers tend to be dominated by the mud fraction, which is transported as wash-load and is notoriously difficult to predict. Instead, riverine sediment concentration, c , is set to be an independent variable and Eqs 1 to 4 are used to predict the lake density required for plunging. Combining Eqs 1 to 4 shows that lake density required for plume plunging is reflective of characteristics of the bedforms deposited near the plunge point represented here by the Yalin number and grain size, which were held constant based on observations from the sand lenses at Pahrump Hills.

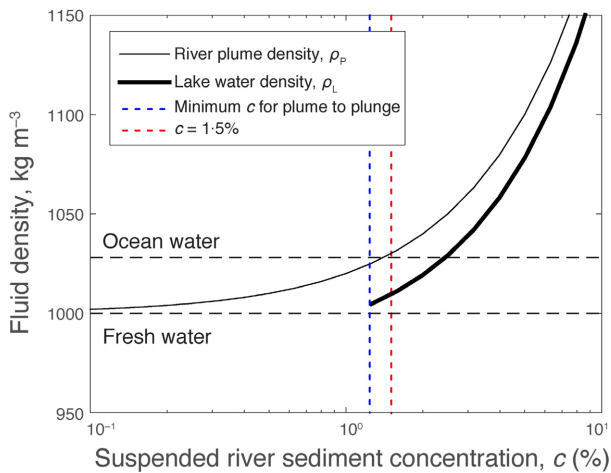


Fig. 20. Fluid density of a modelled river plume as a function of suspended sediment concentration of the river calculated by mass balance via Eq. 4. Also plotted is the lake density in Gale crater as a function of river sediment concentration required for the river plume to plunge and to reach the velocities needed to produce the bedforms observed in sand lenses within the Pahrump Hills section. The blue vertical dashed line represents the minimum suspended river sediment concentration needed for the plume plunge in the Gale crater lake, and also highlights the minimum river plume and lake densities needed for plunging to occur. The red vertical dashed line indicates a suspended river sediment concentration of 1.5%.

Figure 20 shows the generic river plume density, ρ_p , calculated by mass balance via Eq. 4 as a function of the input suspended sediment concentration of the river, c . Also shown in Fig. 20 is predicted lake density, ρ_L , calculated by combining Eqs 1 to 4 and solving for ρ_L as a function of input suspended sediment concentration of the river, c , needed for the plume to plunge. The difference in suspended sediment concentration, c , between these two curves shows the added river sediment concentration needed for a plume both to plunge and to reach the velocities needed to produce the bedforms at the stability threshold between ripples and dunes (Yalin number = 4, grain size of $D = 0.24$ mm) that were observed within the sand lenses at Pahrump Hills. The difference in fluid density, ρ , between these two curves for a given value of c represents the density differential between the river plume and the lake needed for the plume to plunge while also reaching the velocities required to produce the bedforms observed within the Pahrump Hills sand lenses.

The analysis shows that the feeder rivers must have had sediment concentrations that exceeded 1% in order to plunge while also satisfying conditions required to produce the bedforms observed in the sand lenses at Pahrump Hills. Even in a freshwater lake, plumes with $0 < c < 1\%$, despite being denser than the lake water, would not plunge and also produce velocities that explain the observed bedforms in the sand lenses at Pahrump Hills. As the suspended sediment concentration and plume density are increased, the predicted lake density must also increase for the plunging plume velocities to be consistent with the observed bedforms. For example, sediment concentrations of approximately 2.5% produce a plume with density of $\rho_p = 1050$ kg m⁻³ and require a saline lake with a density of $\rho_L = 1028$ kg m⁻³ similar to Earth's oceans to explain the observed bedforms. Salinity levels that exceed ocean water would require river plume sediment concentrations that exceed several percent.

Minimum values measured for suspended sediment concentrations in alluvial rivers on Earth rarely exceed 1.5% (Mulder & Syvitski, 1995). Freshwater river plumes have density equivalence with Earth's oceans with sediment concentration of *ca* 1.4% (Fig. 20), which explains why plunging river plumes are exceedingly rare in the ocean but are common in freshwater lakes and reservoirs (Fan & Morris, 1992; Kostic & Parker, 2003). Mulder & Syvitski (1995) showed that only nine out of 150 rivers analyzed that drain to the ocean are capable of producing plunging plumes annually; and that these nine 'dirty' rivers all have average annual minimum sediment concentrations of $<1.5\%$. Sediment concentrations during extreme flood events (for example, the 100 year flood) can be higher (Mulder and Syvitski, 1995); however, concentrations beyond 10% are unlikely to produce the observed ripple and dune stratification due to buoyancy stratification that suppresses turbulence (Baas *et al.*, 2016).

Due to the ubiquity of possible event beds in the Pahrump Hills member, plunging plumes could have been relatively common and, given minimum sediment concentrations of $<1.5\%$ during typical floods on Earth, this suggests that the lake water had a density near freshwater (Fig. 20). Lake densities greater than Earth's oceans would require sediment concentrations that exceed *ca* 2.5%, which could be possible for more extreme and infrequent flood events. Based on the calculations presented here, lake densities

greater than 1176 kg m^{-3} (corresponding to $c = 10\%$) are unlikely within the Gale crater lake.

IMPLICATIONS OF A HYPERPYCNAL ORIGIN FOR THE HABITABILITY OF GALE CRATER AND OTHER MARTIAN CRATER LAKE DEPOSITS

Several different interpretations have been proposed regarding the salinity of the ancient Gale crater lake recorded in the Pahrump Hills section. The potential for short episodes of evaporation and increased salinity (Kah *et al.*, 2018) recorded in the Pahrump Hills section, or, alternatively, the presence of a deep, saline lake (Schieber *et al.*, 2015) was based on an interpretation of millimetre-scale laths in the basal strata of Pahrump Hills as pseudomorphs after a primary evaporitic phase. Additionally, the presence of hematite and jarosite in the basal Pahrump Hills member, coupled with observed enrichments in Zn, Ni and Mn, have been proposed to possibly represent deposition in an acid saline lake (Rampe *et al.*, 2017). However, Hurowitz *et al.* (2017) proposed that hematite, jarosite and trace mineral enrichments result from oxidative processes in a shallow lacustrine setting, and that chemical and sedimentological features associated with saline fluids resulted from interaction with late diagenetic brines, rather than saline lakewater. Grotzinger *et al.* (2015) also used the lack of primary bedded evaporite deposits and the lack of evidence for sedimentary structures suggestive of subaerial exposure and evaporation to suggest that the ancient lake in Gale crater probably was relatively fresh. The analysis in this study supports a dominantly freshwater interpretation for the ancient Gale crater lake, and suggests that evidence for enhanced salinities would represent, at most, ephemeral episodes – constrained to the lowermost exposed strata – recorded within the Pahrump Hills member.

The presence of a 13 m thick progradational succession at Pahrump Hills recording thousands of laminae, many of which may be individual event beds, suggests that the freshwater lake in Gale crater was relatively stable and long-lived. Whilst accurately determining the time duration represented by this section is impossible without absolute age dates, application of reasonable recurrence intervals for plunging plumes can provide a general constraint. The calculations presented in the previous section support a

freshwater interpretation for the Gale crater lake, suggesting that the conditions necessary for plunging could have been relatively common. If such conditions were achieved seasonally, the section at Pahrump Hills could represent deposition on the order of 10^3 Earth years. If the salinity of the Gale crater lake was closer to that of Earth's oceans, plunging events might have occurred less frequently. Mulder & Syvitski (1995) found that it is common for rivers entering the Earth's oceans to generate hyperpycnal flows at intervals ranging from <100 to 1000 Earth years, with a maximum interval of one flow every 1000 to 10 000 Earth years. If plunging was relatively rare in the Gale crater lake, deposition of the Pahrump Hills section could have spanned up to 10^5 to 10^7 Earth years.

The record of an ancient stable freshwater lake preserved within the Pahrump Hills member has important implications for the sustained habitability of the Gale crater sedimentary succession. Salinity is an important constraint on habitability, since high solute concentrations decrease the availability of water molecules for hydration reactions and may limit cellular function (Grant, 2004; Knoll & Grotzinger, 2004; Tosca *et al.*, 2008; Grotzinger *et al.*, 2014). In this study, the fluid density of the ancient Gale crater lake is constrained to be likely similar to that of freshwater on Earth (*ca* 1000 kg m^{-3}) and most likely no higher than Earth's oceans (1027 kg m^{-3}). This result suggests that the water activity of the ancient Gale crater lake would probably have been conducive to sustained habitable conditions at the surface of Mars during Pahrump Hills member deposition. The first habitable freshwater lacustrine environment explored by the MSL Science Team in the Sheepbed mudstone of Yellowknife Bay (Grotzinger *et al.*, 2014) is *ca* 80 m lower in the stratigraphy than the Pahrump Hills member. Therefore, the presence of these two freshwater lake deposits suggests either a continued record of habitable conditions within Gale crater, or multiple episodes in which habitable conditions were sustained at the surface.

Exploration beyond Pahrump Hills has revealed that the Murray formation extends at least 300 m in thickness (Grotzinger *et al.*, 2015; Fedo *et al.*, 2017, 2018; Rivéra-Hernández *et al.*, 2018). Initial analysis of the overlying Murray formation indicates the recurrence of similar facies as those seen at Pahrump Hills throughout this interval (Fedo *et al.* 2017, 2018) and the analysis presented here can serve as a guide during further refinement of the Murray formation depositional

interpretation. The facies association described for Pahrump Hills may also serve as a reference for the recognition of river-fed crater basin lake deposits by future *in situ* missions to Mars at new landing sites. The Mars 2020 rover mission currently in development is NASA's next flagship Mars rover mission and the first in a series of missions whose goal is to return Mars samples to Earth. The Mars 2020 project is currently considering Jezero crater, an open-basin crater lake site containing a preserved inverted delta and a thick sequence of basin-filling deposits (Fassett & Head, 2005; Goudge *et al.*, 2015, 2017, 2018), as one of three final candidate landing sites. Should Jezero crater be chosen as the landing site for the Mars 2020 rover, the facies associations and depositional model presented here for the Pahrump Hills member – primarily the occurrence of thinly laminated mudstone containing low-angle scour and drape structures interbedded with channelized sand-lenses – could be used as a comparison, enabling the recognition of river-fed lake deposits at the Mars 2020 field area.

CONCLUSIONS

This study presents a depositional model for the Pahrump Hills member of the Murray formation in which thinly laminated mudstones are interpreted to represent deposition of event beds via suspension settling and lofting at the distal margins of river-generated hyperpycnal flows entering an ancient lake in Gale crater. The occurrence of 'scour and drape' structures throughout the thinly laminated mudstone facies favours a subaqueous lacustrine interpretation for the Pahrump Hills member over subaerial alternatives such as airfall of volcanic or aeolian material or aeolian tractional or grainfall deposition. Coarser-grained lenses within the Pahrump Hills succession that exhibit dune and ripple cross-lamination are interpreted to represent predominantly southward transport in shallow subaqueous channelized flows. The occurrence of these channelized deposits in the upper half of the Pahrump Hills section, combined with the overall thickening and coarsening-upward trend observed as the thinly laminated mudstone transitions conformably into planar thick laminated sandstone capping Pahrump Hills, is interpreted as an overall progradational succession. Palaeohydraulic modelling places additional constraints on the salinity of the ancient Gale crater

lake. In order for hyperpycnal flows to plunge and form ripple and dune cross-stratification like that observed in the sandy lenses of Pahrump Hills, the density of the lake body was likely to be similar to that of freshwater on Earth and no denser than Earth's seawater. The presence of thousands of laminae within the Pahrump Hills section supports an overall lake duration likely on the order of *ca* 10³ Earth years, with a maximum possible duration up to *ca* 10⁷ Earth years, consistent with the stability implied by the progradational sequence. These results are consistent with the long-term persistence of an ancient sustained freshwater lake, the key component of the habitable environment described at this site.

ACKNOWLEDGEMENTS

This research was carried out at the Jet Propulsion Laboratory, California Institute of Technology, under a contract with the National Aeronautics and Space Administration. S. Gupta acknowledges funding from the UK Space Agency (UKSA) (Grants ST/J005169/1 and ST/N000579/1). The authors would like to acknowledge the scientists, engineers and management of the MSL mission, without whom the data and analysis presented in this paper would not have been possible. Thanks also to Gilles Dromart and Piret Plink-Björklund for thoughtful reviews that helped to improve this manuscript.

REFERENCES

- Akiyama, J. and Stefan, H.G. (1984) Plunging flow into a reservoir—Theory. *J. Hydraul. Eng.*, **110**, 484–499.
- Anderson, R.Y. and Dean, W.E. (1988) Lacustrine varve formation through time. *Palaeogeogr. Palaeoclimatol. Palaeoecol.*, **62**, 215–235.
- Anderson, R.B. and Bell, J.F., III (2010) Geologic mapping and characterization of Gale crater and implications for its potential as a Mars Science Laboratory landing site. *Mars*, **5**, 76–128.
- Andrews-Hanna, J.C., Soto, A. and Richardson, M.I. (2012) Meridiani planum and gale crater: hydrology and climate of mars at the Noachian-Hesperian boundary. *Lunar Planet. Sci. Conf.*, **43**, 2706.
- Ansari, V., Loizeau, D., Mangold, N., Le Mouélic, S., Carter, J., Poulet, F., Dromart, G., Lucas, A., Bibring, J.-P., Gendrin, A., Gondet, B., Langevin, Y., Masson, P., Murchie, S., Mustard, J.F. and Neukum, G. (2011) Stratigraphy, mineralogy, and origin of layered deposits inside Terby crater, Mars. *Icarus*, **211**, 273–304.
- Antevs, E. (1951) Glacial clays in Steep Rock Lake, Ontario, Canada. *Geol. Soc. Am. Bull.*, **62**, 1223–1262.

- Baas, J.H., Best, J.L. and Peakall, J.** (2016) Predicting bedforms and primary current stratification in cohesive mixtures of mud and sand. *J. Geol. Soc. London*, **173**, 12–25.
- Banham, S.G., Gupta, S., Watkins, J., Edgett, K., Sumner, D., Grotzinger, J.P., Lewis, K., Edgar, L., Stack, K., Barnes, R., Bell, J., Day, M., Ewing, R., Lapotre, M.G.A., Stein, N., Rivera-Hernández, F. and Vasavada, A.** (2018) Sedimentology of an ancient aeolian sandstone on the lower slope of Aeolis Mons: the Stimson formation, Gale crater, Mars. *Sedimentology*, **65**, 993–1042.
- Bell, J.F., III, Godber, A., McNair, S., Caplinger, M.A., Maki, J.N., Lemmon, M.T., Van Beek, J., Malin, M.C., Wellington, D., Kinch, K.M., Madsen, M.B., Hardgrove, C., Ravine, M.A., Jensen, E., Harker, D., Anderson, R.B., Herkenhoff, K.E., Morris, R.V., Cisneros, E. and Deen, R.G.** (2017) The Mars Science Laboratory *Curiosity* rover Mastcam instruments: preflight and in-flight calibration, validation, and data archiving. *Earth Space Sci.*, **4**, 396–452.
- Bennett, K.A. and Bell, J.F., III** (2016) A global survey of martian central mounds: central mounds as remnants of previously more extensive large-scale sedimentary deposits. *Icarus*, **264**, 331–341.
- Bhattacharya, J.P. and MacEachern, J.A.** (2009) Hyperpycnal Rivers and Prodeltaic Shelves in the Cretaceous Seaway of North America. *J. Sed. Res.*, **79**, 184–209.
- Blatt, H., Middleton, G. and Murray, R.** (1972) *Origin of Sedimentary Rocks*, p. 634. Prentice Hall, Englewood Cliffs.
- Bridges, N.T. and Ehlmann, B.L.** (2017) The Mars Science Laboratory (MSL) bagnold dunes campaign, phase 1: overview and introduction to the special issue. *J. Geophys. Res.-Planets*, **123**, 3–19.
- Bridges, N.T., Banks, M.E., Beyer, R.A., Chuang, F.C., Noe Dobrea, E.Z., Herkenhoff, K.E., Keszthelyi, L.P., Fishbaugh, K.E., McEwen, A.S., Michaels, T.I., Thomson, B.J. and Wray, J.J.** (2010) Aeolian bedforms yardangs, and indurated surfaces in the Tharsis Montes as seen by the HiRISE Camera: evidence for dust aggregates. *Icarus*, **205**, 165–182.
- Cabrol, N. and Grin, E.A.** (1999) Distribution classification, and ages of Martian impact crater lakes. *Icarus*, **142**, 160–172.
- Cabrol, N.A. and Grin, E.A.** (2001) The evolution of Lacustrine environments on Mars: is Mars only hydrologically dormant? *Icarus*, **149**, 291–328.
- Cabrol, N.A., Grin, E.A., Newsom, H.E., Landheim, R. and McKay, C.P.** (1999) Hydrogeologic evolution of Gale crater and its relevance to the Exobiological exploration of Mars. *Icarus*, **139**, 235–245.
- Calaf, F.J., III, Dietrich, W.E., Edgar, L., Farmer, J., Fraeman, A., Grotzinger, J., Palucis, M.C., Parker, T., Rice, M., Rowland, S., Stack, K.M., Sumner, D., Williams, J. and the MSL Science Team** (2013) Geologic mapping of the Mars Science Laboratory landing ellipse. *Lunar Planet. Sci. Conf.*, **44**, 2511.
- Cartigny, M.J.B., Postma, G., van den Berg, J.H. and Mastbergen, D.R.** (2011) A comparative study of sediment waves and cyclic steps based on geometries, internal structures, and numerical modeling. *Mar. Geol.*, **280**, 40–56.
- Cartigny, M.J.B., Ventra, D., Postma, G. and van den Berg, J.H.** (2014) Morphodynamics and sedimentary structures of bedforms under supercritical-flow conditions: new insights from flume experiments. *Sedimentology*, **61**, 712–748.
- Cheel, R.J. and Leckie, D.A.** (1993) Hummocky cross-stratification. In: *Sedimentology Review 1* (Ed. V.P. Wright), pp. 103–122. Blackwell Science, Oxford.
- Clemmenson, L.B. and Hegner, J.** (1991) Eolian sequence and erg dynamics; the Permian Corrie Sandstone, Scotland. *J. Sed. Res.*, **61**, 768–774.
- Clifford, S.M. and Parker, T.J.** (2001) The evolution of the Martian hydrosphere: implications for the fate of a primordial ocean and the current state of the northern plains. *Icarus*, **154**, 40–79.
- Davies, N.S. and Gibling, M.R.** (2010) Paleozoic vegetation and the Siluro-Devonian rise of fluvial lateral accretion sets. *Geology*, **38**, 51–54.
- Day, M. and Kocurek, G.** (2016) Observation of an aeolian landscape: from surface to orbit in Gale crater. *Icarus*, **280**, 37–71.
- Day, M., Anderson, W., Kocurek, G. and Mohrig, D.** (2016) Carving intracrater layered deposits with wind on Mars. *Geophys. Res. Lett.*, **43**, 2473–2479.
- de Luca, P.H.V. and Basilici, G.** (2013) A prodeltaic system controlled by hyperpycnal flows and storm waves: reinterpretation of the Punta Negra Formation (Lower-Middle Devonian, Argentine Precordillera). *Brazilian J. Geo.*, **43**, 673–694.
- Di Achille, G. and Hynek, B.M.** (2010) Ancient ocean on Mars supported by global distribution of deltas and valleys. *Nature Geosci.*, **3**, 459–463.
- DiBiase, R.A., Limaye, A.B., Scheingross, J.S., Fischer, W.W. and Lamb, M.P.** (2013) Deltaic deposits at Aeolis Dorsa: sedimentary evidence for a standing body of water on the northern plains of Mars. *J. Geophys. Res.-Planets*, **118**, 1285–1302.
- Dott, R.H., Jr and Bourgeois, J.** (1982) Hummocky stratification: significance of its variable bedding sequences. *Geol. Soc. Am. Bull.*, **93**, 663–680.
- Dromart, G., Quantin, C. and Brouke, O.** (2007) Stratigraphic architectures spotted in Southern Melas Chasma, Valles Marineris, Mars. *Geology*, **35**, 363–366.
- Duke, W.L., Arnett, R.W.C. and Cheel, R.J.** (1992) Shelf sandstones and hummocky cross-stratification: new insights on a stormy debate. *Geology*, **19**, 625–628.
- Edgar, L.A., Grotzinger, J.P., Bell, J.F., III and Hurowitz, J.A.** (2014) Hypotheses for the origin of fine-grained sedimentary rocks at Santa Maria crater, Meridiani Planum. *Icarus*, **234**, 36–44.
- Edgar, L.A., Gupta, S., Rubin, D.M., Lewis, K.W., Kocurek, G.A., Anderson, R.B., Bell, J.F., III, Dromart, G., Edgett, K.S., Grotzinger, J.P., Hardgrove, C., Kah, L.C., Leveille, R., Malin, M.C., Mangold, N., Milliken, R.E., Minitti, M., Palucis, M., Rice, M., Rowland, S.K., Schieber, J., Stack, K.M., Sumner, D.Y., Wiens, R.C., Williams, R.M.E. and Williams, A.J.** (2017) Shaler: *in situ* analysis of a fluvial sedimentary deposit on Mars. *Sedimentology*, **64**, 96–122.
- Edgett, K.S., Yingst, R.A., Ravine, M.A., Caplinger, M.A., Maki, J.N., Tony Ghaemi, F., Schaffner, J.A., Bell, J.F., III, Edwards, L.J., Herkenhoff, K.E., Heydari, E., Kah, L.C., Lemmon, M.T., Minitti, M.E., Olson, T.S., Parker, T.J., Rowland, S.K., Schieber, J., Sullivan, R.J., Sumner, D.Y., Thomas, P.C., Jensen, E.H., Simmonds, J.J., Sengstacken, A.J., Willson, R.G. and Goetz, W.** (2012) *Curiosity's* Mars Hand Lens Imager (MAHLI) Investigation. *Space Sci. Rev.*, **170**, 259–317.
- Edgett, K.S., Caplinger, M.A., Maki, J.N., Ravine, M.A., Tony Ghaemi, F., McNair, S., Herkenhoff, K. E., Duston, B.M., Wilson, R.G., Yingst, R.A., Kennedy, M.R., Minitti, M. E., Sengstacken, A.J., Supulver, K.D., Lipkaman, L.J., Krezoski, G.M., McBride, M.J., Jones, T.L., Nixon, B.E., Van Beek, J.K., Krysak, D.J. and Kirk, R.L.** (2015)

- Curiosity's robotic arm-mounted Mars Hand Lens Imager (MAHLI): Characterization and calibration status. MSL MAHLI Technical Report 0001, <https://doi.org/10.13140/rg.2.1.3798.5447>.
- Ehlmann, B.L., Mustard, J.F., Fassett, C.I., Schon, S.C., Head, J.W., III, Des Marais, D.J., Grant, J.A. and Murchie, S.L. (2008) Clay minerals in delta deposits and organic preservation potential on Mars. *Nature Geosci.*, **1**, 355–358.
- Ewing, R.C., Lapotre, M.G.A., Lewis, K.W., Day, M., Stein, N., Rubin, D.M., Sullivan, R., Banham, S., Lamb, M.P., Bridges, N.T., Gupta, S. and Fischer, W.W. (2017) Sedimentary processes of the Bagnold Dunes: implications for the eolian rock record of Mars. *J. Geophys. Res.-Planets*, **122**, 2544–2573.
- Fan, J. and Morris, G. (1992) Reservoir sedimentation. I: delta and density current deposits. *J. Hydraul. Eng.*, **1183**, 354–369.
- Farmer, J.D. and DesMarais, D.J. (1999) Exploring for a record of ancient Martian life. *J. Geophys. Res.*, **104**, 977–995.
- Farrell, K.M. (1987) Sedimentology and Facies Architecture of Overbank deposits of the Mississippi River, False River Region, Louisiana. In: *Recent Developments in Fluvial Sedimentology* (Eds F.G. Ethridge, R.M. Flores and M.D. Harvey), *SEPM Spec. Publ. No. 39*, pp. 1–48, SEPM, Tulsa, OK.
- Fassett, C.I. and Head, J.W., III (2005) Fluvial sedimentary deposits on Mars: ancient deltas in a crater lake in the Nili Fossae region. *Geophys. Res. Lett.*, **32**, L14201.
- Fassett, C.I. and Head, J.W., III (2008) Valley network-fed, open-basin lakes on Mars: distribution and implications for Noachian surface and subsurface hydrology. *Icarus*, **198**, 37–56.
- Fedo, C., Grotzinger, J., Gupta, S., Stein, N.T., Watkins, J., Banham, S., Edgett, K.S., Minitti, M., Schieber, J., Siebach, K., Stack-Morgan, K., Newsom, H., Lewis, K.W., House, C. and Vasavada, A.R. (2017) Facies analysis and basin architecture of the upper part of the Murray Formation, Gale crater, Mars. *Lunar Planet. Sci. Conf.*, **48**, 1689.
- Fedo, C.M., Grotzinger, J.P., Gupta, S., Fraeman, A., Edgar, L., Edgett, K., Stein, N., Rivera-Hernández, F., Lewis, K., Stack, K.M., House, C., Rubin, D. and Vasavada, A.R. (2018) Sedimentology and stratigraphy of the Murray formation, Gale crater, Mars. *Lunar Planet. Sci. Conf.*, **49**, 2078.
- Fraeman, A.A., Arvidson, R.E., Catalano, J.G., Grotzinger, J.P., Morris, R.V., Murchie, S.L., Stack, K.M., Humm, D.C., McGovern, J.A., Seelos, F.P., Seelos, K.D. and Viviano, C.E. (2012) A hematite-bearing layer in Gale crater, Mars: mapping and implications for past aqueous conditions. *Geology*, **41**, 1103–1106.
- Fraeman, A.A., Ehlmann, B.L., Arvidson, R.E., Edwards, C.S., Grotzinger, J.P., Milliken, R.E., Quinn, D.P. and Rice, M.S. (2016) The stratigraphy and evolution of lower Mount Sharp from spectral, morphological, and thermophysical orbital data sets. *J. Geophys. Res.-Planets*, **121**, 1713–1736.
- Gibling, M.R. (2006) Width and thickness of fluvial channel bodies and valley fills in the geological record: a literature compilation and classification. *J. Sed. Res.*, **76**, 731–770.
- Gibling, M.R., Davies, N.S., Halcon-Lang, H.J., Bashforth, A.R., DiMichele, W.A., Rygel, M.C. and Ielpi, A. (2014) Palaeozoic co-evolution of rivers and vegetation: a synthesis of current knowledge. *Proc. Geol. Assoc.*, **125**, 524–533.
- Goldspiel, J.M. and Squyres, S.W. (1991) Ancient aqueous sedimentation on Mars. *Icarus*, **89**, 392–410.
- Golombek, M., Grant, J., Kipp, D., Vasavada, A., Kirk, R., Ferguson, R., Bellutta, P., Calef, F., Larsen, K., Katayama, Y., Huertas, A., Beyer, R., Chen, A., Parker, T., Pollard, B., Lee, S., Sun, Y., Hoover, R., Sladek, H., Grotzinger, J., Welch, R., Noe Dobrea, E., Michalski, J. and Watkins, M. (2012) Selection of the Mars Science Laboratory landing site. *Space Sci. Rev.*, **170**, 641–737.
- Goudge, T.A., Head, J.W., Mustard, J.F. and Fassett, C.I. (2012) An analysis of open-basin lake deposits on Mars: evidence for the nature of associated lacustrine deposits and post-lacustrine modification processes. *Icarus*, **219**, 211–229.
- Goudge, T.A., Mustard, J.F., Head, J.W., Fassett, C.I. and Wiseman, S.M. (2015) Assessing the mineralogy of the watershed and fan deposits of the Jezero crater paleolake system, Mars. *J. Geophys. Res.-Planets*, **120**, 775–808.
- Goudge, T.A., Milliken, R.E., Head, J.W., Mustard, J.F. and Fassett, C.I. (2017) Sedimentological evidence for a deltaic origin of the western fan deposit in Jezero crater, Mars and implications for future exploration. *Earth Planet. Sci. Lett.*, **458**, 357–365.
- Goudge, T.A., Mohrig, D., Cardenas, B.T., Hughes, C.M. and Fassett, C.I. (2018) Stratigraphy and paleohydrology of delta channel deposits, Jezero crater, Mars. *Icarus*, **301**, 58–75.
- Grant, W.D. (2004) Life at low water activity. *Phil. Trans. Roy. Soc. London*, **359**, 1249–1267.
- Grant, J.A., Wilson, S.A., Mangold, N., Calef, F., III and Grotzinger, J.P. (2014) The timing of alluvial activity in Gale crater, Mars. *Geophys. Res. Lett.*, **41**, 1142–1149.
- Greeley, R. and Guest, J.E. (1987) Geologic map of the eastern equatorial region of Mars. *U.S. Geological Survey Miscellaneous Investigations Series Map I-1802-B*, scale 1: 15,000,000, U.S. Department of the Interior, U.S. Geological Survey.
- Grotzinger, J.P. and Milliken, R.E. (2012) The sedimentary rock record of Mars: distribution, origins, and global stratigraphy. In: *Sedimentary Geology of Mars* (Eds J.P. Grotzinger and R.E. Milliken), *SEPM Spec. Publ. No. 102*, pp. 1–48, SEPM, Tulsa, OK.
- Grotzinger, J.P., Crisp, J., Vasavada, A.R., Anderson, R.C., Baker, C.J., Barry, R., Blake, D.F., Conrad, P., Edgett, K.S., Ferdowski, B., Gellert, R., Gilbert, J.B., Golombek, M., Gómez-Elvira, J., Hassler, D.M., Jandura, L., Litvak, M., Mahaffy, P., Maki, J., Meyer, M., Malin, M.C., Mitrofanov, I., Simmonds, J.J., Vaniman, D., Welch, R.V. and Wiens, R.C. (2012) Mars Science Laboratory mission and science investigation. *Space Sci. Rev.*, **170**, 5–55.
- Grotzinger, J.P., Sumner, D.Y., Kah, L.C., Stack, K., Gupta, S., Edgar, L., Rubin, D., Lewis, K., Schieber, J., Mangold, N., Milliken, R., Conrad, P.G., DesMarais, D., Farmer, J., Siebach, K., Calef, F., Hurowitz, J., McLennan, S.M., Ming, D., Vaniman, D., Crisp, J., Vasavada, A., Edgett, K.S., Malin, M., Blake, D., Gellert, R., Mahaffy, P., Wiens, R.C., Maurice, S., Grant, J.A., Wilson, S., Anderson, R.C., Beegle, L., Arvidson, R., Hallet, B., Sletten, R.S., Rice, M., Bell, J., Griffes, J., Ehlmann, B., Anderson, R.B., Bristow, T.F., Dietrich, W.E., Dromart, G., Eigenbrode, J., Fraeman, A., Hardgrove, C., Herkenhoff, K., Jandura, L., Kocurek, G., Lee, S., Leshin, L.A., Leveille, R., Limonadi, D., Maki, J., McCloskey, S., Meyer, M., Minitti, M., Newsom, H., Oehler, D., Okon, A., Palucis, M., Parker, T., Rowland, S., Schmidt, M., Squyres, S., Steele, A., Stolper, E.,

- Summons, R., Treiman, A., Williams, R. and Yingst, A., MSL Science Team (2014) A Habitable Fluvio-Lacustrine environment at Yellowknife Bay, Gale crater, Mars. *Science*, **343**, 1242777.
- Grotzinger, J.P., Gupta, S., Malin, M.C., Rubin, D.M., Schieber, J., Siebach, K., Sumner, D.Y., Stack, K.M., Vasavada, A.R., Arvidson, R.E., Calef, F., III, Edgar, L., Fischer, W.F., Grant, J.A., Griffes, J., Kah, L.C., Lamb, M.P., Lewis, K.W., Mangold, N., Minitti, M.E., Palucis, M., Rice, M., Williams, R.M., Yingst, R.A., Blake, D., Blaney, D., Conrad, P., Crisp, J., Dietrich, W.E., Dromart, G., Edgett, K.S., Ewing, R.C., Gellert, R., Hurowitz, J.A., Kocurek, G., Mahaffy, P., McBride, M.J., McLennan, S.M., Mischna, M., Ming, D., Milliken, R., Newsom, H., Oehler, D., Parker, T.J., Vaniman, D., Wiens, R.C. and Wilson, S.A. (2015) Deposition, exhumation, and paleoclimate of an ancient lake deposit, Gale crater, Mars. *Science*, **350**, aac7575.
- Harrell, J. (1984) Roller micrometer analysis of grain shape. *J. Sed. Res.*, **54**, 643–645.
- Hays, L.E., Graham, H.V., Des Marais, D.J., Hausrath, E.M., Horgan, B., McCollom, T.M., Paranteau, M.N., Potter-McIntyre, S.L., Williams, A.J. and Lynch, K.L. (2017) Biosignature preservation and detection in mars analog environments. *Astrobiology*, **17**, 363–400.
- Hilliard, J. (1964) Estimating grain size by the intercept method. *Metal Prog.*, **85**, 99–100.
- Hunter, R.E. (1977) Basic types of stratification in small eolian dunes. *Sedimentology*, **24**, 361–387.
- Hunter, R.E. (1981) Stratification styles in eolian sandstones: Some Pennsylvanian to Jurassic examples from the Western Interior U.S.A. *SEPM Special Publication No. 31*, 315–329, <https://doi.org/10.2110/pec.81.31.0315>.
- Hurowitz, J.A., Grotzinger, J.P., Fischer, W.W., McLennan, S.M., Milliken, R.E., Stein, N., Vasavada, A.R., Blake, D.F., Dehouck, E., Eigenbrode, J.L., Fairen, A.G., Frydenvang, J., Gellert, R., Grant, J.A., Gupta, S., Herkenhoff, K.E., Mind, D.W., Rampe, E.B., Schmidt, M.E., Siebach, K.L., Stack-Morgan, K., Sumner, D.Y. and Wiens, R.C. (2017) Redox stratification of an ancient lake in Gale crater, Mars. *Science*, **356**, eaah6849.
- Kah, L.C., Stack, K.M., Eigenbrode, J.L., Yingst, R.A. and Edgett, K.S. (2018) Syndepositional precipitation of calcium sulfate in Gale Crater, Mars. *Terra Nova*, **30**, 431–439.
- Kite, E.S., Lewis, K.W., Lamb, M.P., Newman, C.E. and Richardson, M.I. (2013) Growth and form of the mound in Gale crater, Mars: slope wind enhanced erosion and transport. *Geology*, **41**, 543–546.
- Kite, E.S., Sneed, J., Mayer, D.P., Lewis, K.W., Michaels, T.L., Hore, A. and Rafkin, S.C.R. (2016) Evolution of major sedimentary mounds on Mars: buildup via anitcompensational stacking modulated by climate change. *J. Geophys. Res.-Planets*, **121**, 2282–2324.
- Knoll, A.H. and Grotzinger, J.P. (2004) Water on Mars and the Prospect of Martian, Life. *Elements*, **2**, 169–173.
- Kostic, S. and Parker, G. (2003) Progradational sand–mud deltas in lakes and reservoirs. Part I: theory and numerical model. *J. Hydraul. Res.*, **412**, 127–140.
- Kostic, S. and Parker, G. (2006) The response of turbidity currents to a canyon-fan transition: internal hydraulic jumps and depositional signatures. *J. Hydraul. Res.*, **44**, 631–653.
- Kostic, S. (2011) Modeling of submarine cyclic steps: controls on their formation, migration, and architecture. *Geosphere*, **7**, 294–304.
- Kronyak, R.E., Kah, L.C., Fedo, C.M., Stack, K.M., Edgett, K.S. and Siebach, K.L. (2017) Capping units of the Murray Formation, Gale crater, Mars: salsbery Peak as a Pre-Stimson Formation Caprock. *Lunar Planet. Sci. Conf.*, **48**, 1523.
- Lamb, M.P., Myrow, P.M., Lukens, C., Houck, K. and Strauss, J. (2008) Deposits from wave-influenced turbidity currents: pennsylvanian Minturn Formation, Colorado, USA. *J. Sed. Res.*, **787–8**, 480–498.
- Lamb, M.P., McElroy, B., Kopriva, B., Shaw, J. and Mohrig, D. (2010) Linking river-flood dynamics to hyperpycnal-plume deposits: experiments, theory, and geological implications. *Geol. Soc. Am. Bull.*, **122**, 1389–1400.
- Lapotre, M.G.A., Lamb, M. and McElroy, B. (2017) What sets the size of current ripples? *Geology*, **45**, 243–246.
- Lazar, O.R., Bohacs, K.M., Macquaker, J.H.S., Schieber, J. and Demko, T.M. (2015) Capturing key attributes of fine-grained sedimentary rocks in outcrops, cores, and thin sections: nomenclature and description guidelines. *J. Sed. Res.*, **84**, 230–246.
- Le Deit, L., Hauber, E., Fueten, F., Pondrelli, M., Pio Rossi, A. and Jaumann, R. (2013) Sequence of infilling events in Gale crater, Mars: results from morphology, stratigraphy, and mineralogy. *J. Geophys. Res.-Planets*, **118**, 2439–2473.
- Le Mouélic, S., Gasnault, O., Herkenhoff, K.E., Bridges, N.T., Langevin, Y., Mangold, N., Maurice, S., Wiens, R.C., Pinet, P., Newsom, H.E. and Deen, R.G. (2015) The ChemCam Remote Micro-Imager at Gale crater: review of the first year of operations on Mars. *Icarus*, **249**, 93–107.
- Lee, H.Y. and Yu, W.S. (1997) Experimental study of reservoir turbidity current. *J. Hydraul. Eng.*, **123**, 520–528.
- Lewis, K.W. and Aharonson, O. (2006) Stratigraphic analysis of the distribution fan in Eberswalde crater using stereo imagery. *J. Geophys. Res.-Planets*, **111**, E06001.
- Long, D.G.F. (2011) Architecture and depositional style of fluvial systems before land plants: a comparison of Precambrian, Early Paleozoic, and Modern River Deposits. In: *From River to Rock Record: The Preservation of Fluvial Sediments and Their Subsequent Interpretation* (Eds: S.K. Davidson, S. Leleu and C.P. North), *SEPM Special Publication No. 97*, pp. 37–61, SEPM, Tulsa, OK.
- Maki, J., Thiessen, D., Pourangi, A., Kobzeff, P., Litwin, T., Scherr, L., Elliott, S., Dingizian, A. and Maimone, M. (2012) The Mars Science Laboratory engineering cameras. *Space Sci. Rev.*, **170**, 77–93.
- Malin, M.C. and Edgett, K.S. (2000) Sedimentary rocks of early Mars. *Science*, **290**, 1927–1937.
- Malin, M.C., Ravine, M.A., Caplinger, M.A., Ghaemi, F.T., Schaffner, J.A., Maki, J.N., Bell, J.F., III, Cameron, J.F., Dietrich, W.E., Edgett, K.S., Edwards, L.J., Garvin, J.B., Hallet, B., Herkenhoff, K.E., Heydari, E., Kah, L.C., Lemmon, M.T., Minitti, M.E., Olson, T.S., Parker, T.J., Rowland, S.K., Schieber, J., Sletten, R., Sullivan, R.J., Sumner, D.Y., Yingst, R.A., Duston, B.M., McNair, S. and Jensen, E.H. (2017) The Mars Science Laboratory (MSL) Mast cameras and Descent imager: investigation and instrument descriptions. *Earth Space Sci.*, **4**, 506–539.
- Mangold, N., Thompson, L.M., Forni, O., Williams, A.J., Fabre, C., Le Deit, L., Wiens, R.C., Williams, R., Anderson, R.B., Blaney, D.L., Calef, F., Cousin, A., Clegg, S.M., Dromart, G., Dietrich, W.E., Edgett, K.S., Fisk, M.R., Gasnault, O., Gellert, R., Grotzinger, J.P., Kah, L., Le Mouélic, S., McLennan, S.M., Maurice, S., Meslin, P.-Y., Newsom, H.E., Palucis, M.C., Rapin, W., Sautter, V., Siebach, K.L., Stack, K., Sumner, D. and Yingst, A. (2016)

- Composition of conglomerates analyzed by the *Curiosity* rover: implications for Gale crater crust and sediment sources. *J. Geophys. Res.-Planets*, **121**, 353–387.
- Martínez, G.M., Newman, C.N., de Vicente-Retortillo, A., Fischer, E., Renno, N.O., Richardson, M.I., Fairén, A.G., Genzer, M., Guzewich, S.D., Haberle, R.M., Harri, A.-M., Kempainen, O., Lemmon, M.T., Smith, M.D., de la Torre-Juárez, M. and Vasavada, A.R. (2017) The modern near-surface martian climate: a review of in-situ meteorological data from Viking to Curiosity. *Space Sci. Rev.*, **212**, 295–338.
- Maurice, S., Wiens, R.C., Saccoccio, M., Barraclough, B., Gasnault, O., Forni, O., Mangold, N., Baratoux, D., Bender, S., Berger, G., Bernardin, J., Berthe, M., Bridges, N., Blaney, D., Bouye, M., Cais, P., Clark, B., Clegg, S., Cousin, A., Cremers, D., Cros, A., DeFlores, L., Derycke, C., Dingler, B., Dromart, G., Dubois, B., Dupieux, M., Durand, E., d'Uston, C., Fabre, C., Faure, B., Gaboriaud, A., Gharsa, T., Herkenhoff, K., Kan, E., Kirkland, L., Kouach, D., Lacour, J.-L., Langevin, Y., Lasue, J., Le Mouélic, S., Lescure, M., Lewin, E., Limonadi, D., Manhès, G., Mauchien, P., McKay, C., Meslin, P.-Y., Michel, Y., Miller, E., Newsom, H.E., Ortnner, G., Paillet, A., Parés, L., Parot, Y., Pérez, R., Pinet, P., Poitrasson, F., Quertier, B., Sallé, B., Sotin, C., Sautter, V., Séran, H., Simmonds, J.J., Sirven, J.-B., Stiglich, R., Striebig, N., Thocaven, J.-J., Toplis, M.J. and Vaniman, D. (2012) The ChemCam instrument suite on the Mars Science Laboratory (MSL) Rover: science objectives and mast unit description. *Space Sci. Rev.*, **170**, 95–166.
- McBride, M.J., Miniti, M.E., Stack, K.M., Yingst, R.A., Edgett, K.S., Goetz, W., Herkenhoff, K.E., Heydari, E., Kah, L.C., Rowland, S.K., Schieber, J., Harker, D., Kennedy, M.R., Krezoski, G.M., Lipkamin, L., Nixon, B. and Van Beek, J. (2015) Mars Hand Lens Imager (MAHLI) Observations at the Pahrump Hills Field Site, Gale crater. *Lunar Planet. Sci. Conf.*, **46**, 2855.
- McMahon, W.J. and Davies, N.S. (2018) Evolution of alluvial mudrock forced by early land plants. *Science*, **359**, 1022–1024.
- Metz, J.M., Grotzinger, J.P., Mohrig, D., Milliken, R., Prather, B., Pirmoze, C., McEwen, A.S. and Weitz, C.M. (2009) Sublacustrine depositional fans in southwest Melas Chasma. *J. Geophys. Res.-Planets*, **114**, E10002.
- Milliken, R.E., Ewing, R.C., Fischer, W.W. and Hurowitz, J. (2014) Wind-blown sandstones cemented by sulfate and clay minerals in Gale Crater, Mars. *Geophys. Res. Lett.*, **41**, 1149–1154.
- Milliken, R.E., Grotzinger, J.P. and Thomson, B.J. (2010) Paleoclimate of Mars as captured by the stratigraphic record in Gale crater. *Geophys. Res. Lett.*, **37**, L04201. <https://doi.org/10.1029/2009GL041870>.
- Morgan, A.M., Wilson, S.A., Howard, A.D., Craddock, R.A. and Grant, J.A. (2018) Global distribution of Alluvial fans and deltas on Mars. *Lunar Planet. Sci. Conf.*, **49**, 2219.
- Mulder, T. and Syvitski, J.P.M. (1995) Turbidity currents generated at river mouths during exceptional discharges to the world oceans. *J. Geol.*, **103**, 285–299.
- Mulder, T. and Alexander, J. (2001) The physical character of subaqueous sedimentary density flows and their deposits. *Sedimentology*, **48**, 269–299.
- Mulder, T., Syvitski, J.P.M., Migeon, S., Faugeres, J.C. and Savoye, B. (2003) Marine hyperpycnal flows: initiation, behavior and related deposits: a review. *Mar. Petrol. Geol.*, **20**, 861–882.
- Mutti, E., Davoli, G., Tinterri, R. and Zavala, C. (1996) The importance of ancient fluvio-deltaic systems dominated by catastrophic flooding in tectonically active basins. *Mem. di Sci. Geol.*, **48**, 233–291.
- Myrow, P.M., Lamb, M.P., Lukens, C., Houck, K. and Strauss, J. (2008) Proximal to distal facies relationships in deposits of wave-influenced hyperpycnal flows. In: *Sediment transfer from shelf to deepwater—Revisiting the delivery mechanisms* (Eds J.J. Ponce and E.B. Olivero), Conference Proceedings, AAPG Hedberg Conference, 5 p.
- Olariu, C., Steel, R.J. and Petter, A.L. (2010) Delta-front hyperpycnal bed geometry and implications for reservoir modeling: cretaceous Panther Tongue delta, Book Cliffs, Utah. *AAPG Bull.*, **94**, 819–845.
- Palucis, M.C., Dietrich, W.E., Hayes, A.G., Williams, R.M.E., Gupta, S., Mangold, N., Newsom, H., Hardgrove, C., Calef, F., III and Sumner, D.Y. (2014) The origin and evolution of the Peace Vallis fan system that drains to the Curiosity landing area, Gale crater, Mars. *J. Geophys. Res.-Planets*, **119**, 705–728.
- Parker, T.J., Saunders, R.S. and Schneeberger, D.M. (1989) Transitional morphology in west Deuteronilus Mensae, Mars – Implications for modification of the lowland upland boundary. *Icarus*, **82**, 111–145.
- Parker, T.J., Gorsline, D.S., Saunders, R.S., Pieri, D.C. and Schneeberger, D.M. (1993) Coastal geomorphology of the Martian northern plains. *J. Geophys. Res.*, **98**, 11061–11078.
- Parker, G. and Toniolo, H. (2007) Note on the analysis of plunging of density flows. *J. Hydraul. Eng.*, **133**, 690–694.
- Perron, J.T., Mitrovica, J.X., Manga, M., Matsuyama, I. and Richards, M.A. (2007) Evidence for an ancient Martian ocean in the topography of deformed shorelines. *Nature*, **447**, 840–843.
- Postma, G., Kleverlaan, K. and Cartigny, M.J.B. (2014) Recognition of cyclic steps in sandy and gravelly turbidite sequences and consequences for the Bouma facies model. *Sedimentology*, **61**, 2268–2290.
- Powers, M.C. (1953) A new roundness scale for sedimentary particles. *J. Sed. Res.*, **23**, 117–119.
- Rampe, E.B., Ming, D.W., Blake, D.F., Bristow, T.F., Chipera, S.J., Grotzinger, J.P., Morris, R.V., Morrison, S.M., Vaniman, D.T., Yen, A.S., Achilles, C.N., Craig, P.I., Des Marais, D.J., Downs, R.T., Farmer, J.D., Fendrich, K.V., Gellert, R., Hazen, R.M., Kah, L.C., Morookian, J.M., Peretyazhko, T.S., Sarrazin, P., Treiman, A.H., Berger, J.A., Eigenbrode, J., Fairén, A.G., Forni, O., Gupta, S., Hurowitz, J.A., Lanza, N.L., Schmidt, M.E., Siebach, K., Sutter, B. and Thompson, L.M. (2017) Mineralogy of an ancient lacustrine mudstone succession from the Murray formation, Gale crater, Mars. *Earth Planet. Sci. Lett.*, **471**, 172–185.
- Rice, M.S., Bell, J.F., III, Gupta, S., Warner, N.H., Goddard, K. and Anderson, R.B. (2013) A detailed geologic characterization of Eberswalde crater, Mars. *Mars*, **8**, 15–57.
- Rice, M.S., Gupta, S., Treiman, A.H., Stack, K.M., Calef, F., Edgar, L.A., Grotzinger, J., Lanza, N., Le Deit, L., Lasue, J., Siebach, K.L., Vasavada, A., Wiens, R.C. and Williams, J. (2017) Geologic overview of the Mars Science Laboratory rover mission at the Kimberley, Gale crater, Mars. *J. Geophys. Res.-Planets*, **122**, 2–20.
- Rivéra-Hernandez, F., Sumner, D.Y., Mangold, N., Stack, K.M., Edgett, K., Stein, N., Heydari, E., Fedo, C., Banham, S.G., Gupta, S., Schieber, J., Newsom, H., Forni, O., Yingst, A., Nachon, M., L'Haridon, J., Gasnault, O.,

- Wiens, R. and Maurice, S. (2018) Characterizing shifting ancient depositional environments in the Murray formation, Gale crater, Mars from ChemCam LIBS Data. *Lunar Planet. Sci. Conf.*, **49**, 2973.
- Rogers, A.D., Warner, N.H., Golombek, M.P., Head, J.W., III and Cowart, J.C. (2018) Areally extensive surface Bedrock exposures on Mars: many are Clastic Rocks, not Lavas. *Geophys. Res. Lett.*, **45**, 1767–1777.
- Rossi, A.P., Neukum, G., Pondrelli, M., vanGasselt, S., Zegers, T., Hauber, E., Chicarro, A. and Foing, B. (2008) Large-scale spring deposits on Mars? *J. Geophys. Res.*, **113**, E08016.
- Schieber, J., Sumner, D., Bish, D., Stack, K., Minitti, M., Yingst, A., Edgett, K., Malin, M., Grotzinger, J. and the MSL Team (2015) The Pahrump succession in gale crater —A potentially evaporite bearing lacustrine mudstone with resemblance to earth analogs. *Lunar Planet. Sci. Conf.*, **46**, 2153.
- Schon, S.C., Head, J.W. and Fassett, C.I. (2012) An overfilled lacustrine system and progradational delta in Jezero crater, Mars: implications for Noachian climate. *Plan. Space Sci.*, **67**, 28–45.
- Scott, D.H., Morris, E.C. and West, M.N. (1978) Geologic map of the Aeolis quadrangle of Mars. *United States Geological Survey Miscellaneous Investigations Series, Map I-1111*, scale 1: 5,000,000, U.S. Department of the Interior, U.S. Geological Survey.
- Scott, D.H. and Chapman, M.G. (1995) Geologic and topographic maps of the Elysium Paleolake basin, Mars. *United States Geological Survey Miscellaneous Investigations Series, Map I-2397*, scale 1: 5,000,000, U.S. Department of the Interior, U.S. Geological Survey.
- Sequeiros, O.E., Spinewine, B., Beaubouef, R.T., Sun, T., Garcia, M.H. and Parker, G. (2010) Bedload transport and bed resistance associated with density and turbidity currents. *Sedimentology*, **57**, 1463–1490.
- Sharp, R.P. (1973) Mars: troughed Terrain. *J. Geophys. Res.*, **78**, 4063–4072.
- Siebach, K.L., Baker, M.B., Grotzinger, J.P., McLennan, S.M., Gellert, R., Thompson, L.M. and Hurowitz, J.A. (2017) Sorting out compositional trends in sedimentary rocks of the Bradbury group (Aeolus Palus). Gale crater, Mars. *J. Geophys. Res.-Planets*, **122**, 295–328.
- Smiley, T.L. (1955) Varve studies. In: *Geochronology* (Ed: T.L. Smiley), *Univ. Arizona Phys. Sci. Bull.*, **2**, pp. 135–150.
- Stack, K.M. (2015) *Reconstructing Past Depositional and Diagenetic Processes through Quantitative Stratigraphic Analysis of the Martian Sedimentary Rock Record*. Dissertation (Ph.D.), California Institute of Technology, <https://doi.org/10.7907/z9fn144m>.
- Stack, K.M., Edwards, C.S., Grotzinger, J.P., Gupta, S., Sumner, D.Y., Calef, F.J., III, Edgar, L.A., Edgett, K.S., Fraeman, A.A., Jacob, S.R., Le Deit, L., Lewis, K.W., Rice, M.S., Rubin, D., Williams, R.M.E. and Williford, K.H. (2016) Comparing orbiter and rover image-based mapping of an ancient sedimentary environment, Aeolis Palus, Gale crater, Mars. *Icarus*, **280**, 3–21.
- Stack, K.M., Cofield, S.M. and Fraeman, A.A. (2017) Geologic map of the MSL *Curiosity* rover extended mission traverse of Aeolis Mons, Gale crater, Mars. *Lunar Planet. Sci. Conf.*, **48**, 1889.
- Sturm, M. and Matter, A. (1978) Turbidites and varves in Lake Brienz (Switzerland): deposition of clastic detritus by density currents. *Spec. Publs int. Ass. Sediment.*, **2**, 147–168.
- Summons, R.E., Amend, J., Buick, R., Bish, D., Cody, G., Des Marais, D., Dromart, G., Eigenbrode, J. and Knoll, A. (2011) Preservation of Martian organic and environmental records: final report of the Mars Biosignature Working Group. *Astrobiology*, **11**, 157–181.
- Sumner, E.J., Amy, L.A. and Talling, P.J. (2008) Deposit structure and processes of sand deposition from decelerating sediment suspensions. *J. Sed. Res.*, **78**, 529–547.
- Szabó, T., Domokos, G., Grotzinger, J.P. and Jerolmack, D.J. (2015) Reconstructing the transport history of pebbles on Mars. *Nature Commun.*, **6**, 8366.
- Thomson, B.J., Bridges, N.T., Milliken, R., Bell, J.F., III, Calvin, W.C. and Weitz, C.M. (2008) New constraints on the origin and evolution of the layered deposits in Gale crater, Mars. *Lunar Planet. Sci. Conf.*, **39**, 1456.
- Thomson, B.J., Bridges, N.T., Milliken, R.E., Baldrige, A., Hook, S.J., Crowley, J.K., Marion, G.M., de Souza Filho, C.R., Brown, A.J. and Weitz, C.M. (2011) Constraints on the origin and evolution of the layered mound in Gale crater, Mars using Mars Reconnaissance Orbiter Data. *Icarus*, **214**, 413–432.
- Tosca, N.J., Knoll, A.H. and McLennan, S.M. (2008) Water activity and the challenge for life on early Mars. *Science*, **320**, 1204–1207.
- Vasavada, A.R., Grotzinger, J.P., Arvidson, R.E., Calef, F.J., Crisp, J.A., Gupta, S., Hurowitz, J., Mangold, N., Maurice, S., Schmidt, M.E., Wiens, R.C., Williams, R.M.E. and Yingst, R.A. (2014) Overview of the Mars Science Laboratory mission: bradbury landing to Yellowknife Bay and beyond. *J. Geophys. Res.-Planets*, **119**, 1134–1161.
- Warner, N., Gupta, S., Lin, S.Y., Kim, J.-R., Muller, J.-P. and Morley, J. (2010) Late Noachian to Hesperian climate change on mars: evidence of episodic warming from transient crater lakes near Ares Vallis. *J. Geophys. Res.-Planets*, **115**, E06013. <https://doi.org/10.1029/2009JE003522>.
- Watkins, J., Grotzinger, J., Stein, N., Banham, S.G., Gupta, S., Rubin, D., Stack, K.M. and Edgett, K.S. (2016) Paleotopography of erosional unconformity, base of the Stimson formation, Gale crater, Mars. *Lunar Planet. Sci.*, **47**, 2939.
- Wentworth, C.K. (1922) A scale of grade and class terms for clastic sediments. *J. Geol.*, **30**, 377–392.
- Williams, R.M.E., Grotzinger, J.P., Dietrich, W.E., Gupta, S., Sumner, D.Y., Wiens, R.C., Mangold, N., Malin, M.C., Edgett, K.S., Maurice, S., Forni, O., Gasnault, O., Ollila, A., Newsom, H.E., Dromart, G., Palucis, M.C., Yingst, R.A., Anderson, R.B., Herkenhoff, K.E., Le Mouélic, S., Goetz, W., Madsen, M.B., Koefoed, A., Jensen, J.K., Bridges, J.C., Schwenzer, S.P., Lewis, K.W., Stack, K.M., Rubin, D., Kah, L.C., Bell, J.F., Farmer, J.D., Sullivan, R., Van Beek, T., Blaney, D.L., Pariser, O. and Deen, R.G. (2013) Martian fluvial conglomerates at Gale crater. *Science*, **340**, 1068–1072.
- Wright, L.D., Wiseman, W.J., Bornhold, B.D., Prior, D.B., Suhayda, J.N., Keller, G.H., Yang, Z.S. and Fan, Y.B. (1988) Marine dispersal and deposition of Yellow-River silts by gravity-driven underflows. *Nature*, **332**, 629–632.
- Yingst, R.A., Edgett, K.S., Kennedy, M.R., Krezoski, G.M., McBride, M.J., Minitti, M.E., Ravine, M.A. and Williams, R.M.E. (2016) MAHLI on Mars: lessons learned operating

a geoscience camera on a landed payload robotic arm. *Geosci. Instrum. Method. Data Syst.*, **5**, 205–217.

Zavala, C., Ponce, J.J., Arcuri, M., Drittanti, D., Freije, H. and Asensio, M. (2006) Ancient lacustrine hyperpycnites: a depositional model from a case study in the Rayoso Formation (Cretaceous) of West-Central Argentina. *J. Sed. Res.*, **76**, 41–59.

Zavala, C., Arcuri, M., Di Meglio, M., Gamero Diaz, H. and Contreras, C. (2011) A genetic facies tract for the analysis of sustained hyperpycnal flow deposits. In: *Sediment Transfer from Shelf to Deep Water—Revisiting the Delivery System* (Eds. R.M. Slatt and C. Zavala), *AAPG Studies in Geology*, **61**, 31–51.

Manuscript received 3 June 2018; revision accepted 1 November 2018

Supporting Information

Additional information may be found online in the Supporting Information section at the end of the article:

Appendix S1. Naming Conventions.

Appendix S2. Grain Size Measurements.

Figure S2-1. Grain shape traces (yellow) from a MAHLI

z-stack image of the Salsberry Peak Kanosh cobble near Pahrump Hills (0942MH0001630000303662R00) fit with minimum bounding geometry (MBG) rectangles (red).

Figure S2-2. Relative proportions of grains (red portion of the circle) and matrix (yellow portion of the circle) measured in Sierra Nevada MAHLI z-stack (MH0004580000302120R00) via the circular intercept method.

Appendix S3. Lamination Thickness Measurements.

Figure S3-1. Locations of laminae measurements at Pahrump Hills outcrop. (A) Annotated thickness measurements (cyan) for laminations within the Pelona target at Shoemaker.

Table S2-1. Grain-size measurements from the thickly laminated mudstone–sandstone facies measured in a MAHLI z-stack image (0942MH0001630000303662R00) at the Kanosh cobble Devils Punchbowl target.

Table S2-2. Lengths of the Hilliard circles attributable to individual grains versus matrix unresolvable in MAHLI images.

Table S2-3. Grain diameter measurements from MAHLI image (0831MH0001700000301828R00) for the Goldstone target in the Chinle area.

Table S3-1. Laminae thickness measurements at Pahrump Hills.